Available online at www.sciencedirect.com

ScienceDirect

Underground Space 27 (2026) 278–300

www.keaipublishing.com/undsp

Research Paper

Bearing capacity and mechanical properties of tunnel anchorage layer under full-face and large-face excavation

Henghong Yang [a,b], Mingnian Wang [a,b,*], Li Yu [a,b], Jie Liu [a,b], Xiao Zhang [a,b], Zhihui Xu [a,b], Jun Liu [a,b]

[a] *School of Civil Engineering, Southwest Jiaotong University, Chengdu 610036, China*
[b] *Key Laboratory of Traffic Tunnel Engineering Ministry of Education, Southwest Jiaotong University, Chengdu 610036, China*

Received 19 May 2025; received in revised form 15 September 2025; accepted 8 October 2025
Available online 14 January 2026

Abstract

With the development of large-scale mechanized construction techniques, tunnel excavation is predominantly executed using either full-face or large-face methods, often supplemented with anchor-bolt reinforcement. However, the reinforcement mechanism of prestressed anchor bolts and the impact of excavation methods on the anchorage layer are yet to be comprehensively clarified through an integrated lens that bridges the macroscopic bearing capacity with mesoscopic mechanical properties. In this study, diverse support types and excavation methods were considered to perform a comprehensive series of loading and failure tests on tunnel anchorage layers. Through the incorporation of stress monitoring, P-wave velocity analysis, and particle image velocimetry (PIV), this study revealed the reinforcement mechanisms of prestressed anchor bolts. In parallel, it delineates the influence of excavation methods on both the macroscopic bearing capacity and mesoscopic mechanical properties of the anchorage layer. The experimental findings revealed that prestressed anchor-bolt reinforcement induced a progressive evolution in the surrounding rock, characterized by sequential modifications in stress, integrity, mechanical properties, ductility, and bearing capacity. Relative to the unsupported conditions, the prestressed anchor-bolt reinforcement yielded substantial enhancements: stress improved by approximately 245.5%, integrity by 14.3%, mechanical properties by 9.8%, ductility by 147.7%, and bearing capacity by up to 500%. In unsupported conditions or with anchor bolts, large-face excavation demonstrated superior performance relative to full-face excavation, enhancing both the mesoscopic mechanical properties and macroscopic bearing capacity by approximately 2.8%–6.9% and 50%–100%, respectively. The findings indicate that large-face excavation is the preferred method under these support conditions. However, when prestressed anchor-bolt reinforcement is used, the differences between the two construction methods become negligible, rendering full-face excavation the more practical construction option.

Keywords: Anchorage layer; Full-face excavation; Large-face excavation; Macroscopic bearing capacity; Mesoscopic mechanical property

1 Introduction

With the rapid advancement of mechanized and intelligent construction technologies, both the scale and frequency of tunnel engineering projects have expanded markedly. In the context of large-scale mechanized excavation, two principal methods are typically employed: full-face and large-face excavation methods, the latter of which retains the tunnel invert during the excavation process. However, owing to the expansive excavation span and rapid construction pace of both methods, tunnels are susceptible to large deformations, rockfalls, collapses, and other failures (Wei & Zhu, 2021). Anchor-bolt reinforcement is routinely employed to mitigate construction-induced risk. Once installed, the anchor bolts integrate with the surrounding rock mass to form a unified structure,

* Corresponding author at: School of Civil Engineering, Southwest Jiaotong University, Chengdu 610036, China.
E-mail address: wmn00525@my.swjtu.edu.cn (M. Wang).
Peer review under the responsibility of Tongji University

https://doi.org/10.1016/j.undsp.2025.10.008

termed the anchorage layer, which collectively sustains external loads and markedly enhances the overall stability of the surrounding rock. To enhance construction safety without compromising efficiency and to enable the precise and optimized design of anchor bolts, the reinforcement mechanisms of anchor bolts and the influence of excavation methods on the macroscopic and mesoscopic perspectives within the anchorage layer must be characterized.

Several studies have aimed to characterize the reinforcement mechanisms, bearing capacities, and mechanical properties of anchorage layers. With respect to reinforcement mechanisms, anchor bolts primarily stabilize weak surrounding rock by suspending unstable rock masses and preventing rockfalls or collapses (Elrawy et al., 2020; Martin, 2012). Supporting this view, theoretical models have been developed to determine the minimum anchor bolt length required to effectively mobilize this suspension effect (He et al., 2015). Beyond this fundamental function, anchor bolts optimize the stress distribution within the rock mass (Chen et al., 2016; Hyett et al., 1992), resulting in stress arches and beam effects that collectively enhance the overall stability of the surrounding rock (Hoek & Brown, 1980; Lang, 1961; Singh et al., 2020; Skrzypkowski et al., 2020; Yang et al., 2025). In addition, anchor bolts impart confinement to the surrounding rock mass (Sun et al., 2022; Wang et al., 2018), with the magnitude of this confinement influence intensifying with the number of installed anchor bolts (Chen et al., 2018; Deb & Das, 2011).

With regard to the bearing capacity and mechanical properties of the anchorage layer, numerous studies have demonstrated that anchor reinforcement enhances the shear strength and bearing capacity of the surrounding rock at the macroscopic scale, with these improvements being strongly influenced by the length of the installed anchor bolts (Chen et al., 2020; Dong & Wang, 2020; Høien et al., 2021). Variations in the anchor bolt diameter and ambient temperature can significantly affect the failure mechanisms of an anchoring system, thereby altering its overall bearing performance (Hu et al., 2023; Liu et al., 2023; Zuo et al., 2019). The confining pressure and interfacial friction at the rock–anchor interface play a pivotal role in modulating the anchorage performance and governing the stress distribution along the anchor bolt (Ho et al., 2019; Ma et al., 2019). From a mesoscopic perspective, anchor-bolt reinforcement enhances the elastic modulus and the cohesion of the surrounding rock (Srivastava & Singh, 2015; Yu et al., 2023). With increasing anchor bolt density, the uniaxial compressive, tensile, and biaxial compressive strengths of the rock exhibit marked enhancements, although their evolution does not conform to a strictly linear trend (Li et al., 2017). Notably, larger crossing angles between the jointed rock mass and anchor bolt tend to yield more pronounced reinforcement effects (Jing et al., 2014). Through homogenization, the anchor–rock composite can be regarded as an equivalent continuum material with improved and uniformly distributed mechanical properties (Carranza-Torres, 2009). Despite the considerable body of research dedicated to elucidating the reinforcement mechanisms of anchor bolts and the bearing capacity and mechanical properties of the anchoring layer, several critical limitations persist.

(1) Existing studies generally characterize anchor-bolt reinforcement as an increase in bearing capacity at the macroscopic scale and improvements in stress and mechanical properties at the mesoscopic scale. However, the reinforcement mechanism has not been comprehensively elucidated from the perspective of rock mass integrity, nor has it been examined through a unified framework that explicitly links macroscopic bearing behavior with mesoscopic mechanical properties. To address this limitation, the present study incorporates P-wave velocity measurements into physical model experiments to quantitatively evaluate rock mass integrity. By grounding the analysis in rock integrity evolution, the reinforcement mechanism of anchor bolts is systematically interpreted across macroscopic and mesoscopic scales.
(2) Although previous research confirms that anchor-bolt reinforcement enhances the mechanical properties of surrounding rock, the fundamental mechanisms driving these improvements remain insufficiently explained. In this study, the reinforcement mechanism is clarified through the lens of rock integrity, tracing a continuous progression from stress redistribution to integrity enhancement and, ultimately, to the strengthening of mechanical properties.
(3) With respect to the factors influencing the bearing capacity and mechanical properties of the anchorage layer, existing studies have predominantly focused on parameters such as anchor bolt length, spacing, and density, typically within the framework of a single anchor bolt interacting with the surrounding rock. However, the influence of excavation methods on the macroscopic bearing capacity and mesoscopic properties of the entire tunnel anchorage layer remains insufficiently understood. Moreover, systematic guidance on selecting optimal excavation methods for different support conditions has yet to be established. Accordingly, this study conducts experiments on the entire tunnel anchorage layer, incorporating full-face and large-face excavation methods commonly used in practice. The results elucidate the influence of excavation methods on the macroscopic bearing capacity and the mesoscopic mechanical properties of the tunnel anchorage layer under varying support types, thereby offering practical guidance for excavation strategies in tunnels constructed with different support types.

To address these research gaps, the tunnel anchorage layer is isolated as an independent structural system and

subjected to a series of loading and failure experiments to investigate its macroscopic bearing capacity and mesoscopic mechanical properties. The experimental program considers multiple excavation methods and support types and employs advanced monitoring techniques, including P-wave velocity measurement and particle image velocimetry (PIV). Section 2 presents a detailed description of the experimental setup, Sections 3 and 4 analyze the macroscopic and mesoscopic experimental results, respectively, and Section 5 discusses the reinforcement mechanisms of anchor bolts and the effects of excavation methods on the anchorage layer.

2 Experimental setup

2.1 Similarity ratio and experimental system

2.1.1 Similarity ratio and tunnel cross-section

The fundamental similarity ratios employed in the experiment encompass geometry C_L, gravity C_γ, strain C_ε, Poisson's ratio C_v, and P-wave velocity $C_{V\mathrm{p}}$. Among these, the C_L value is 45, while the C_γ, C_ε, C_v, and $C_{V\mathrm{p}}$ values are maintained at 1. The remaining similarity parameters are listed in Table 1.

The experiment utilized a 350 km/h double-track railway tunnel as the prototype cross-section, adhering to the specifications outlined in the Chinese industrial standard TB 10621—2014 (National Railway Administration of the People's Republic of China, 2014) for high-speed rail infrastructure. The tunnel features a cross-sectional profile with a height of 12.54 m and a span of 14.86 m. To investigate the bearing capacity and mechanical properties of the tunnel anchorage layer under conditions of full-face excavation (including tunnel invert excavation) and large-face excavation (excluding tunnel invert excavation), the corresponding full-face and large-face tunnel cross-sections were derived in accordance with the prescribed geometric similarity ratio, as illustrated in Fig. 1. In the experimental model, the tunnel span for the full-face cross-section measures 0.33 m, with a height of 0.28 m, and excludes the presence of a tunnel invert at the base, as depicted in Fig. 1(a). The large-face cross-section, derived from the full-face cross-section, incorporates a 0.06 m high tunnel invert at the base, as illustrated in Fig. 1(b).

In practical tunnel engineering, the anchorage layer typically consists of the surrounding rock and reinforcing anchor bolts. To faithfully reproduce actual engineering scenarios, the model tests employed similar materials to represent both the surrounding rock and reinforcing anchor bolts, in line with the established practice in previous experimental investigations of the anchorage layer (Xiao et al., 2024; Yang et al., 2025). Moreover, the selection of similar materials is governed by the prescribed similarity ratios derived from the physical and mechanical properties of the surrounding rock and anchor bolts. This approach ensures that the anchorage layer in the model test not only preserves fidelity to actual tunnel engineering but also yields meaningful comparability in terms of both macroscopic bearing capacity and mesoscopic mechanical properties. To quantitatively assess the bearing capacity of the anchorage layer under both full-face and large-face excavation strategies, a 0.09-m-thick anchorage layer was delineated, corresponding to the length of the anchor bolts employed in the experiment. The surrounding rock within the anchorage layer was infilled to simulate the in situ conditions. Beyond the anchorage layer, rounded fine-grained yellow sand was employed as the filling medium for two reasons. First, its distinct color contrast with the surrounding rock materials facilitates the clear visual identification of anchorage layer phenomena, such as deformation, rock detachment, and collapse, during loading. If the exterior is filled with materials resembling the surrounding rock, the boundaries between the anchorage layer and the host medium would become indistinct, complicating the accurate evaluation of the bearing capacity of the anchorage layer. Second, owing to its smooth surface and high compactibility, the round fine-grained yellow sand effectively transmits the applied load to the anchorage layer. Accordingly, in line with previous research on anchorage layer model testing (Xiao et al., 2024; Yang et al., 2025), this study adopted round, fine-grained yellow sand as the external fill.

2.1.2 Experimental system

This experiment was designed as a plane strain test, wherein longitudinal effects were neglected. The dimensions of the model box measured 0.8 m × 1.1 m, as illustrated in Fig. 2. The model box was enclosed by steel plates, and its front panel was constructed from transparent organic glass to facilitate observation. The experimental apparatus comprised two jacks: a laptop for data acquisition, a spotlight for enhanced visibility, a high-resolution camera for detailed documentation, and a stress–strain gauge for precise measurements.

Table 1
Similarity ratio design.

Parameter	Geometry	Stress	Strain	Gravity	P-wave velocity	Elastic modulus	Poisson's ratio	Friction angle	Cohesion
Similarity ratio	1:45	1:45	1:1	1:1	1:1	1:45	1:1	1:1	1:45

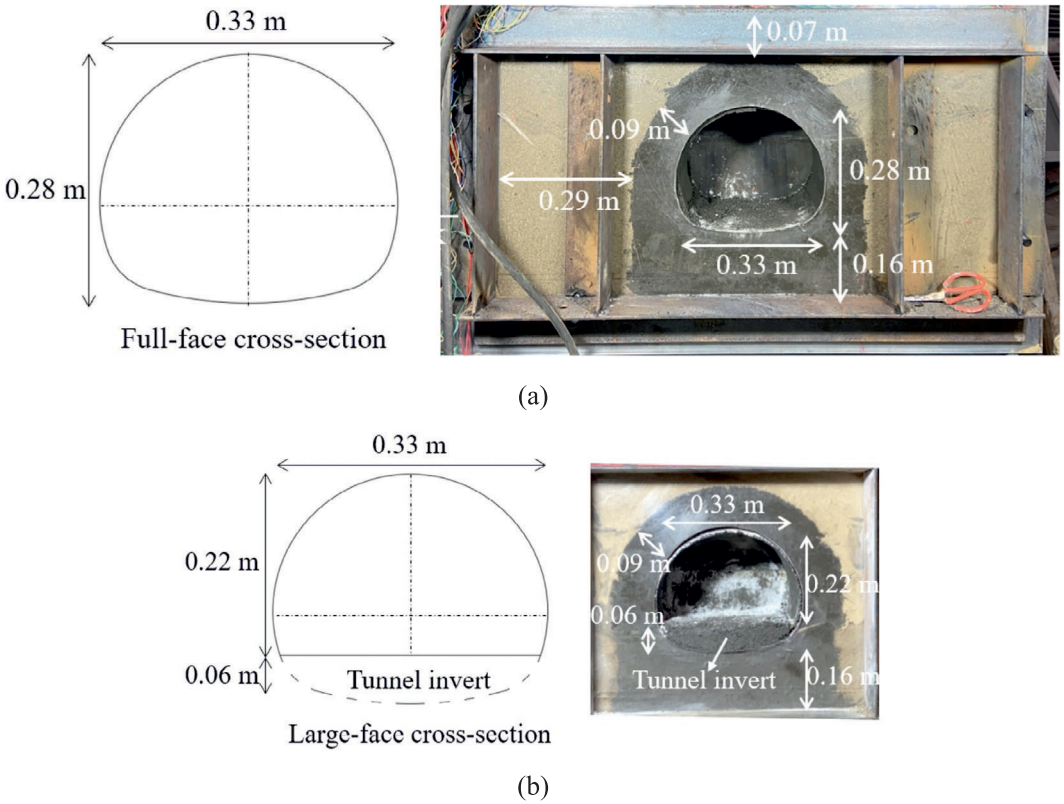

Fig. 1. Tunnel cross-section. (a) Full-face excavation, and (b) large-face excavation.

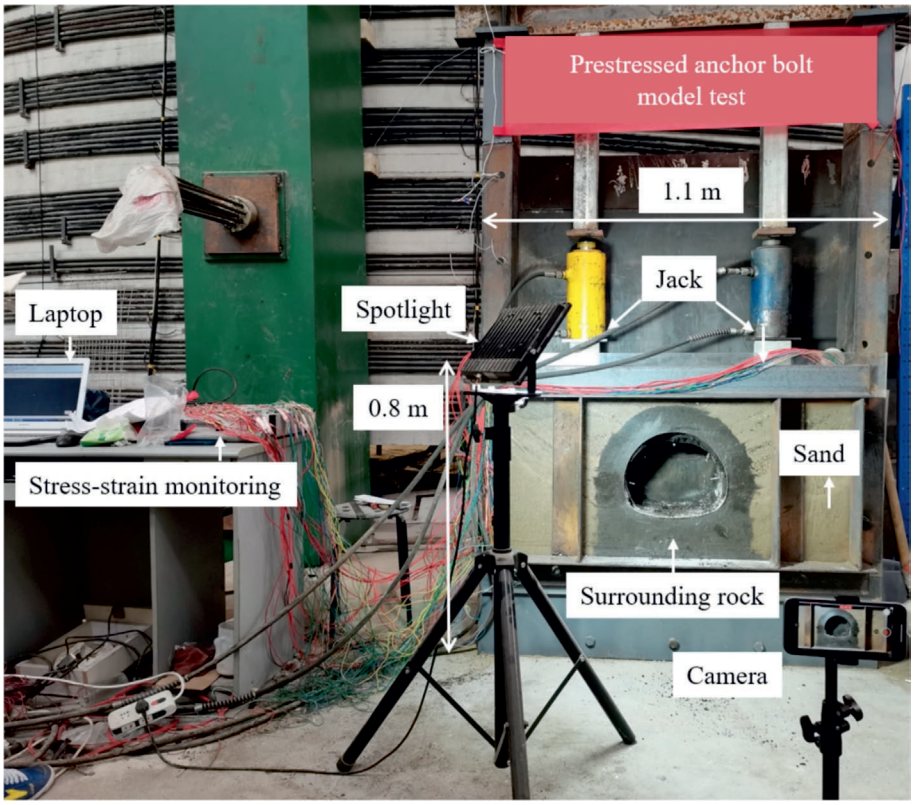

Fig. 2. Experimental system.

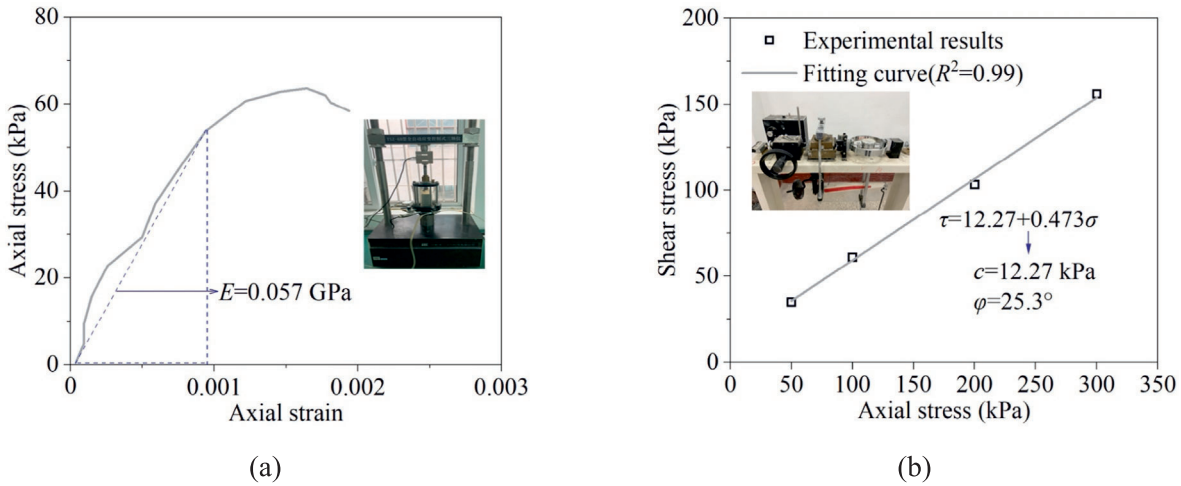

(a) (b)

Fig. 3. Surrounding rock. (a) Deformation parameter, and (b) strength parameter.

2.2 Similarity materials

2.2.1 Surrounding rock

Building on the research of Tang et al. (2023), similar materials replicating the surrounding rock were formulated by blending fly ash, river sand, and oil in a controlled ratio to ensure consistency and stability. The deformation and strength parameters were determined through triaxial and direct shear tests, as shown in Fig. 3. Following an iterative refinement process, the optimal mixing ratio for the surrounding rock material was determined as fly ash:river sand:oil = 4.8:4.2:1. The corresponding mechanical parameters are listed in Table 2. τ and σ are the shear stress and axial stress, respectively. c and φ are the cohesion and friction angle of the surrounding rock similarity material, respectively.

2.2.2 Bolt

In the experiment, a threaded rod was employed to simulate the anchor bolt, ensuring appropriate stiffness contrast with the surrounding rock. The simulation and installation procedures for the anchor bolts are shown in Fig. 4. Prestressing was introduced through a combination of gaskets, springs, and strip caps, with a pre-embedded installation method adopted to enhance structural integrity. To increase frictional resistance, the surface of the anchor bolt was coated with quartz sand. The anchor bolt had a diameter of 1.8 mm and was arranged at a spacing of 0.033 m. The total length of the threaded rod measures 0.13 m, with 0.09 m representing the embedded portion that simulates the anchor bolt, while the remaining 0.04 m is designated for the application of prestress.

2.2.3 Sand

In the experiment, sand primarily served as a medium for load transfer. To ensure uniformity and reliability, naturally rounded fine sand was selected and meticulously sieved using a 2 mm aperture. The deformation and strength parameters of sand were determined through triaxial and direct shear tests, and the results are presented in Fig. 5 and Table 3.

2.3 Monitoring plan

2.3.1 Stress–strain

The stress distribution within the surrounding rock was monitored using soil pressure cells strategically positioned at critical locations, including the tunnel crown, shoulder, hance, and foot, with 21 measurement points, as illustrated in Fig. 6. TC-1 denotes the measurement point along the tunnel crown contour, and TC-3 corresponds to the monitoring point at the interface between the surrounding rock and the anchorage layer of the tunnel crown.

2.3.2 P-wave velocity

To capture the mesoscopic mechanical properties of the anchorage layer, a P-wave velocity monitoring system was integrated into the experiment to assess the integrity of the surrounding rock, as shown in Fig. 7. Initially, five transducers, referred to as pre-embedded transducers, were

Table 2
Mechanical parameters of the surrounding rock similarity material.

Item		Density (kg/m^3)	Elastic modulus (GPa)	Possion's ratio	Cohesion (kPa)	Friction angle (°)
Surrounding rock	Model test	2010	0.057	0.34	12.27	25.3
	Prototype	2100	2	0.35	585	25
Similarity ratio		1.04	35.09	1.03	47.68	0.99

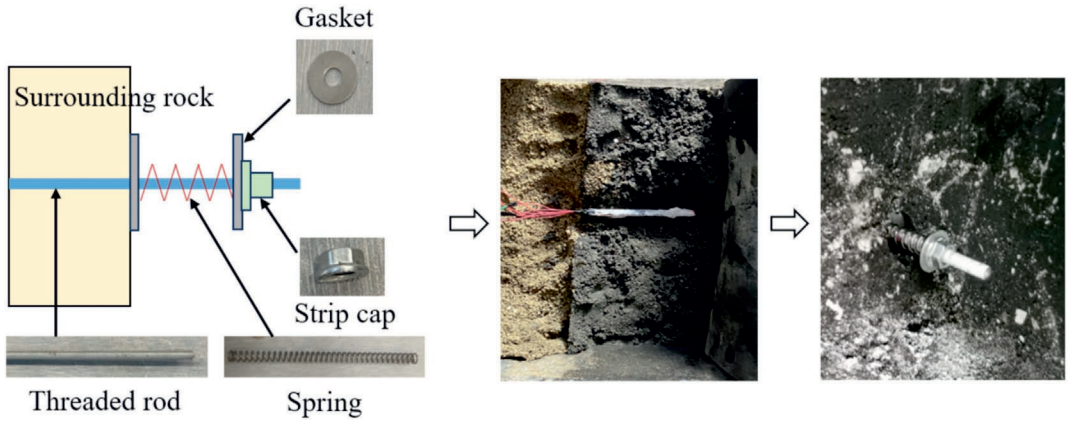

Fig. 4. Simulation and installation of a prestressed anchor bolt.

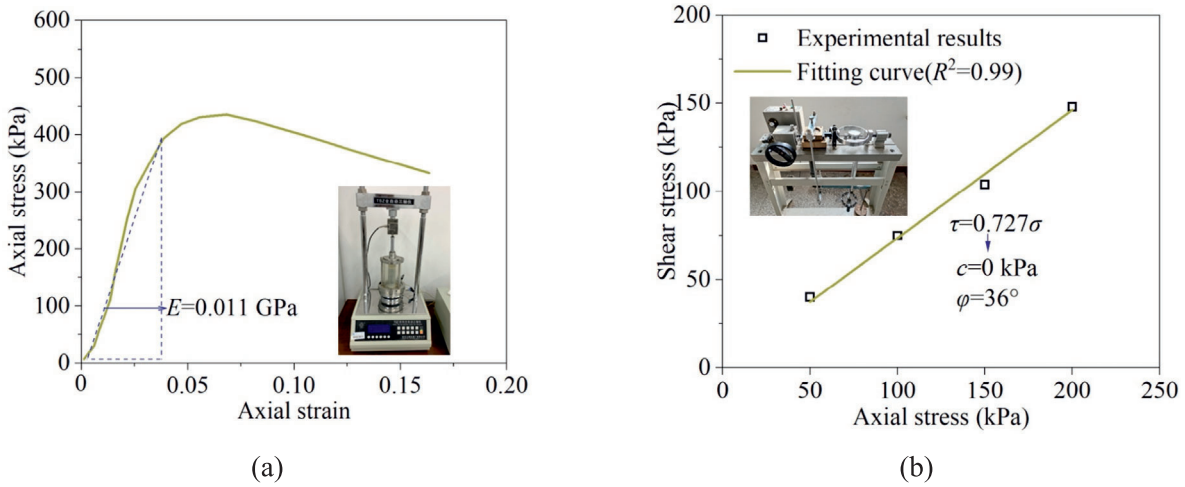

Fig. 5. Sand. (a) Deformation parameter, and (b) strength parameter.

Table 3
Mechanical parameters of sand similarity material.

Item		Density (kg/m^3)	Elastic modulus (GPa)	Possion's ratio	Cohesion (kPa)	Friction angle (°)
Sand	Model test	1780	0.011	0.35	0	36
	Prototype	1800	0.015	0.34	0	35
Similarity ratio		1.01	1.36	0.97	45	0.97

strategically positioned within the tunnel crown, shoulder, and hance. During testing, a moving transducer, in conjunction with a digital measurement instrument and pre-embedded transducers, was employed to accurately determine the P-wave velocity of the surrounding rock. A compact rock specimen with a length of 10 cm was prepared to determine the intrinsic P-wave velocity of the surrounding rock, as illustrated in Fig. 8. The measured value of the P-wave velocity V_{p0} was 2137 m/s. Based on Eq. (1), the integrity index K_v of the surrounding rock was calculated.

$$K_v = \left(\frac{V_p}{V_{p0}}\right)^2, \quad (1)$$

where V_p is the P-wave velocity of the surrounding rock, V_{p0} is the P-wave velocity of the intrinsic surrounding rock, and K_v is the integrity of the surrounding rock.

2.3.3 Displacement

To capture the displacement of the surrounding rock with high precision, a noncontact particle image velocimetry (PIV) technique was employed. PIV is a displacement measurement technique based on optical imaging and image correlation analysis. Its underlying principle involves capturing sequential images embedded with tracer particles or natural surface textures and applying cross-correlation algorithms to resolve the collective translation of particle

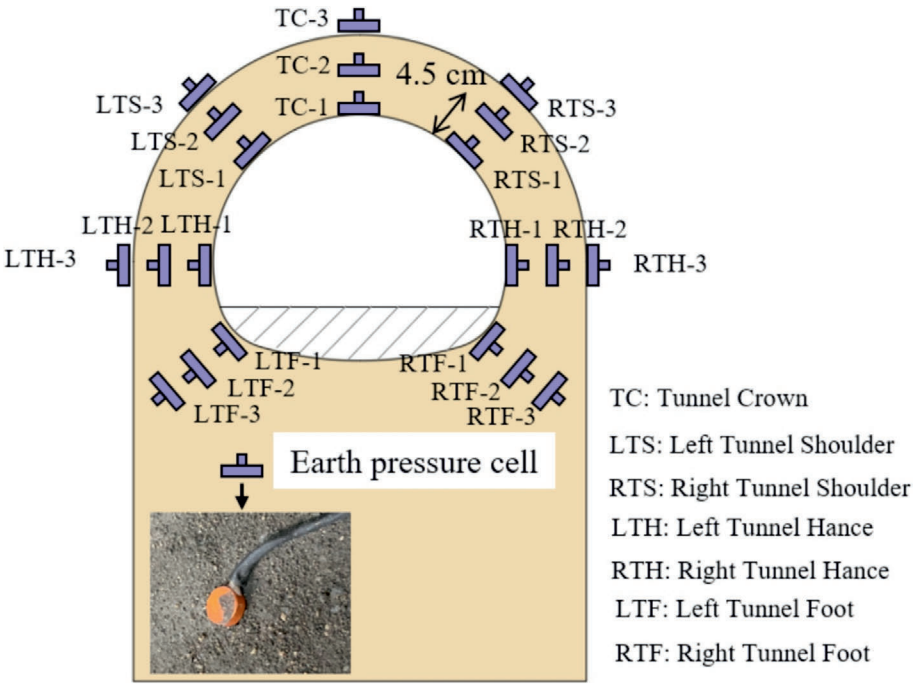

Fig. 6. Stress–strain monitoring.

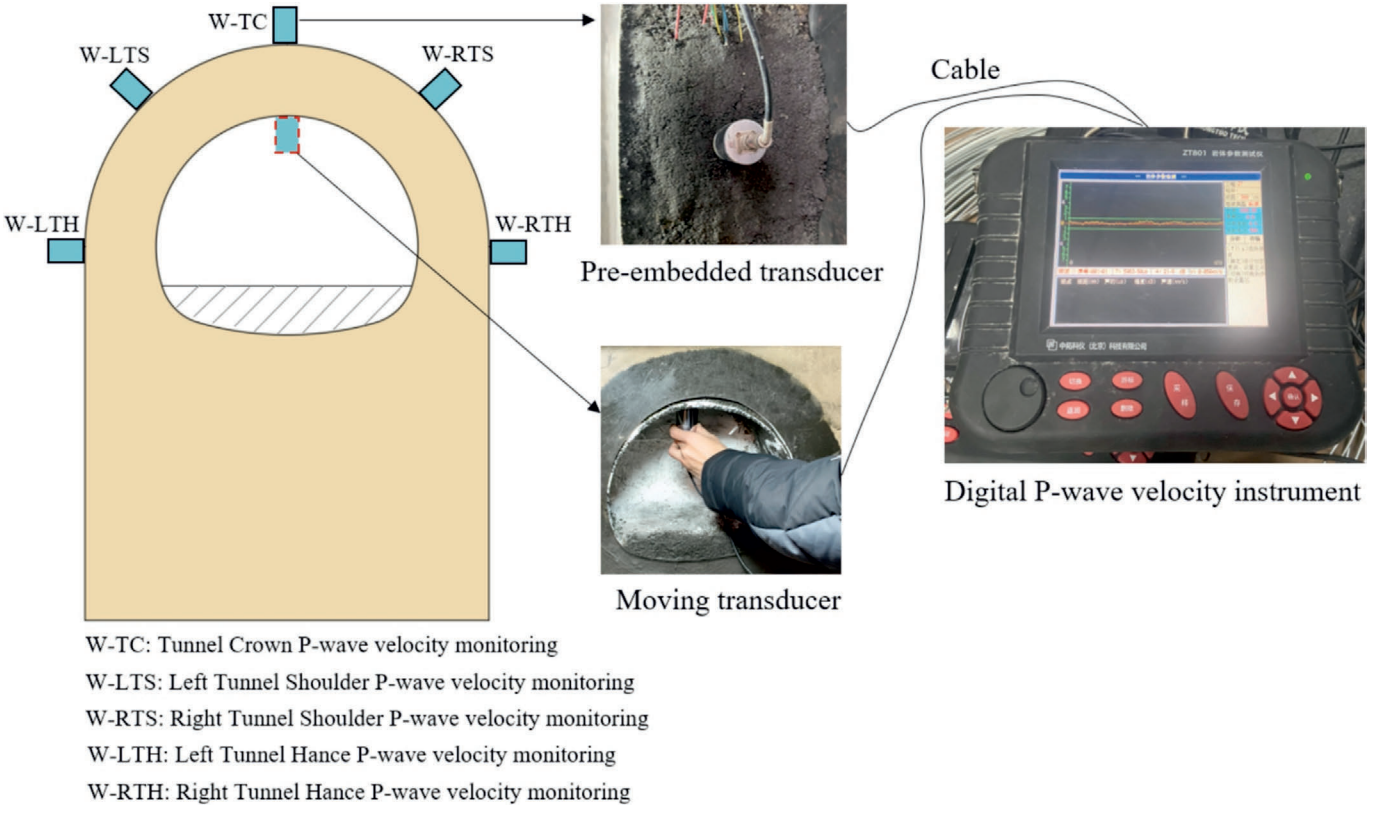

Fig. 7. P-wave velocity monitoring.

ensembles between successive frames, thereby deriving local displacement vectors. By integrating these vectors through full-field reconstruction, a continuous displacement distribution is obtained, enabling high-resolution, noncontact characterization of structural or material deformation. The PIV system comprised spotlights, cameras, and model boxes, as shown in Fig. 9. The optical center of the camera was aligned horizontally with the

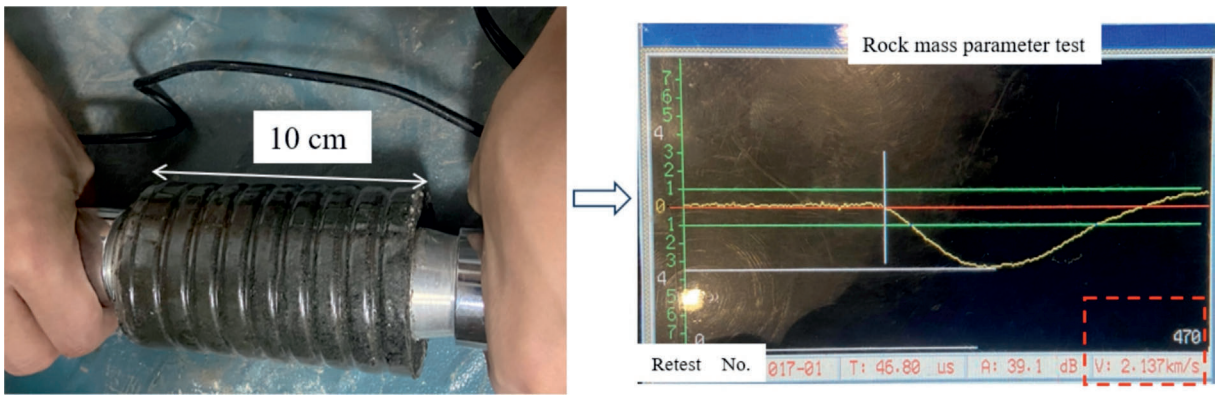

Fig. 8. Measurement of V_{p0}.

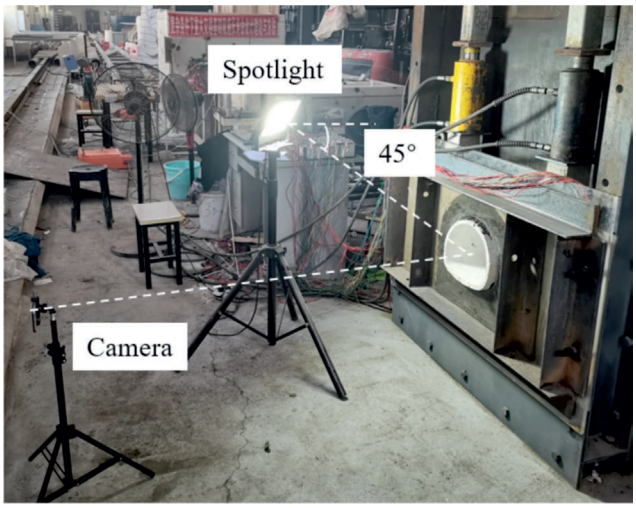

Fig. 9. Displacement monitoring.

midpoint of the tunnel section, and the spotlight was positioned at a 45° angle to ensure uniform illumination. High-resolution images of the surrounding rock were captured using the camera and subsequently processed using the open-source platform PIVlab (Thielicke & Stamhuis, 2014), enabling the extraction of displacement fields with high accuracy.

2.4 Work conditions and test procedure

To investigate the evolution of both the macroscopic bearing capacity and microscopic mechanical properties of the tunnel anchorage layer under full-face and large-face excavations, accounting for variations in the support types and excavation methods, six distinct test conditions were established, as summarized in Table 4.

The test procedure comprises the following five sequential steps:

(1) Establish connections between the laptop and various sensors, including soil pressure cells and static strain gauges, to ensure data acquisition and monitoring.
(2) Fill the model box with the designated similar materials, ensuring adherence to the excavation conditions; for the full-face excavation, the tunnel invert was omitted, whereas for the large-face excavation, it was retained. Concurrently, pre-embed soil pressure cells, P-wave velocity transducers, and anchor bolts at their designated monitoring points to facilitate precise data acquisition. Given the experimental isolation of the anchorage layer, a support lining must be incorporated during the filling process to prevent structural collapse and maintain the integrity of the anchorage layer.
(3) Position the camera and spotlight in accordance with the predefined configuration of the PIV system.
(4) Carefully remove the support lining and proceed with the installation of the spring, gasket, and strip cap to effectively apply the prestress to the anchor bolt.
(5) Pretesting indicated that the anchorage layer typically underwent deformation, rock detachment, and eventual stabilization within approximately 15 min of each load application. Accordingly, loads were

Table 4
Work conditions.

Test No.	Support type	Excavation method	Remark
1	–	Full-face	Surrounding rock layer with full-face excavation (SRL-F)
2	Anchor bolt	Full-face	Anchorage layer with full-face excavation (AL-F)
3	Prestressed anchor bolt	Full-face	Prestressed anchorage layer with full-face excavation (PAL-F)
4	–	Large-face	Surrounding rock layer with large-face excavation (SRL-L)
5	Anchor bolt	Large-face	Anchorage layer with large-face excavation (AL-L)
6	Prestressed anchor bolt	Large-face	Prestressed anchorage layer with large-face excavation (PAL-L)

applied to the tunnel anchorage layer at 20-min intervals, with increments of 20 kPa per step, until anchorage layer failure occurred.

2.5 Numerical validation

2.5.1 Model establishment

To validate the experimental findings, numerical models were constructed using FLAC2D, with the experimental conditions PAL-F and PAL-L selected as representative cases, as illustrated in Fig. 10. The numerical model was assigned material mechanical properties, boundary conditions, geometric dimensions, and loading schemes consistent with those of the physical experiments. The base of the model was constrained as fixed, the top surface was treated as free, and the remaining boundaries were subjected to normal constraints. In alignment with the experimental test, each loading step was set at 20 kPa. Given the inability of finite element analysis to reproduce rockfall, the ultimate applied loads were defined as 100 kPa for both PAL-F and PAL-L, corresponding to their respective failure load σ_f. In the numerical model, both the sand and surrounding rock were characterized using the Mohr–Coulomb failure criterion and modeled using zone elements in FLAC. Prestressed anchor bolts were represented through cable elements. The simulation was performed in four stages: initial stress equilibrium, tunnel excavation, installation of prestressed anchor bolts, and subsequent loading.

2.5.2 Results validation

As exemplified by TC-2, the evolution of radial stress for PAL-F and PAL-L, obtained from both the numerical simulations and physical model experiments, is presented in Fig. 11(a) and (b), and the corresponding radial stress distributions are illustrated in Fig. 11(c) and (d). As loading progressed, the radial stress exhibited a steady increase. Numerical simulations and model experiments demonstrated strong concordance in both the evolutionary trends and magnitudes of the measured values. At a loading level of $\sigma = 100$ kPa, the numerical radial stress at TC-2 for PAL-F was 35.4 kPa, compared with an experimental value of 39.8 kPa, yielding a deviation of 12.4%. For PAL-L, the numerical result was 40.1 kPa, while the experimental value was 41.2 kPa, corresponding to an error of only 2.7%. These results confirm the reliability and validity of the experimental model.

3 Macroscopic experimental results

3.1 Failure process

The failure process of the SRL under both the full-face and large-face excavations is illustrated in Fig. 12. In the SRL-F configuration, a rockfall of 3.8 cm × 1.2 cm was observed at the left tunnel shoulder, while a larger rockfall of 6.2 cm × 1.8 cm occurred at the right tunnel shoulder when subjected to a load of $\sigma = 20$ kPa. In contrast, the SRL-L configuration exhibited a rockfall of 6.5 cm × 1.4 cm at the left tunnel shoulder under $\sigma = 40$ kPa. These observations indicate that structural failure in the SRL-F case was initiated at 20 kPa, whereas in the SRL-L case, failure commenced at 40 kPa. As the applied load increased, the failure progress in both SRL-F and SRL-L extended toward the tunnel crown. Under $\sigma = 40$ kPa, SRL-F exhibited a rockfall of 10.2 cm × 3.4 cm at the tunnel crown, whereas SRL-L experienced a comparatively smaller rockfall of 4.8 cm × 2.9 cm at $\sigma = 60$ kPa. Subsequently, structural failure in both cases propagated laterally along the tunnel profile. At $\sigma = 60$ kPa, SRL-F underwent further rockfalls of 11.6 cm × 2.2 cm at the left tunnel shoulder, 8.8 cm × 1.1 cm at the right tunnel shoulder, and 8.6 cm × 1.5 cm at the right tunnel hance.

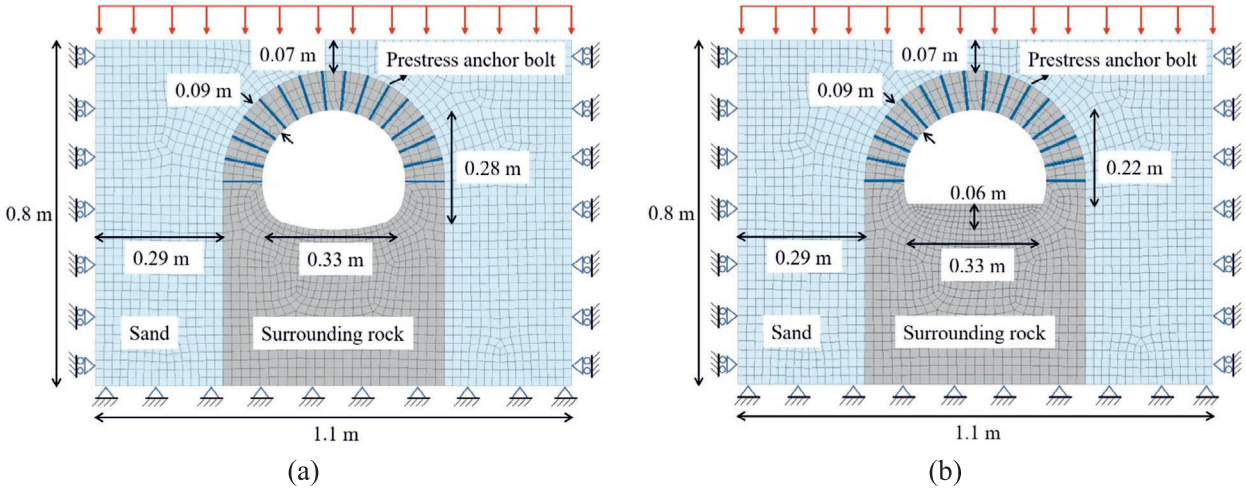

Fig. 10. Numerical model. (a) PAL-F, and (b) PAL-L.

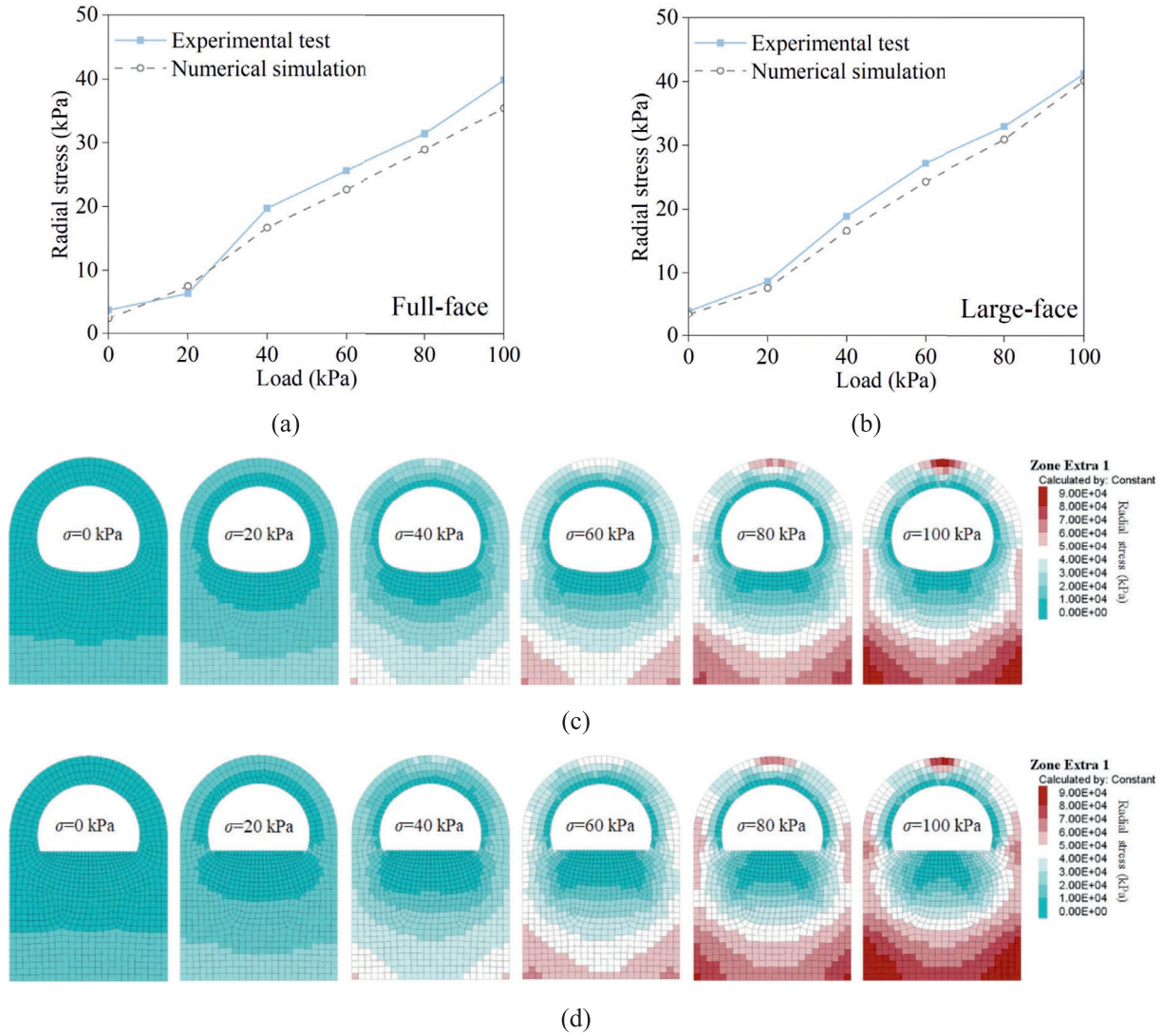

Fig. 11. Radial stress. (a) PAL-F validation, (b) PAL-L validation, (c) cloud chart of PAL-F, and (d) cloud chart of PAL-L.

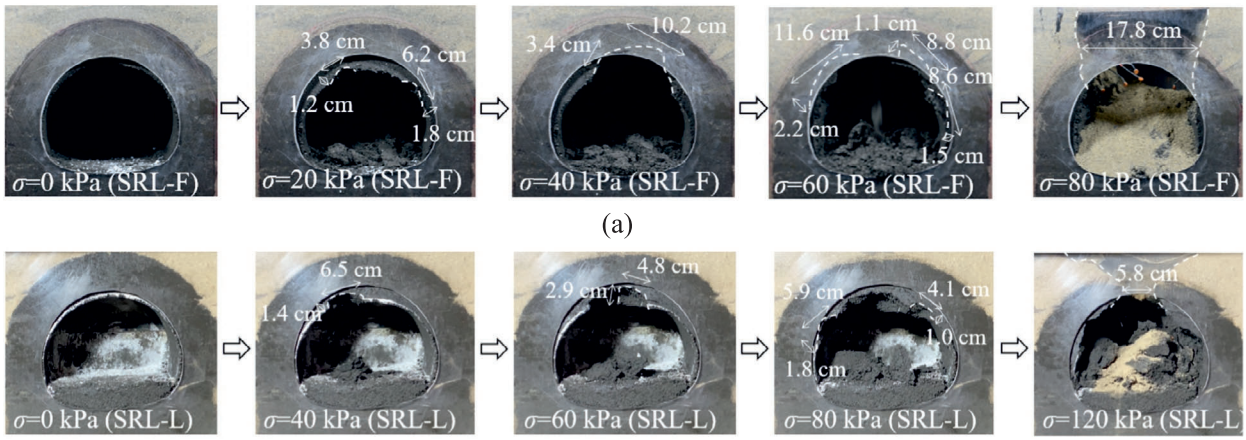

Fig. 12. Failure process of SRL. (a) SRL-F, and (b) SRL-L.

In contrast, at $\sigma = 80$ kPa, SRL-L exhibited rockfalls of 5.9 cm × 1.8 cm at the left tunnel hance and 4.1 cm × 1.0 cm at the right tunnel shoulder. The ultimate failure of the SRL manifested as a collapse at the tunnel crown. In the SRL-F configuration, structural failure occurred under a load of 80 kPa, with a collapse width of 17.8 cm. In contrast, SRL-L withstood a higher load of 120 kPa before succumbing to failure, exhibiting a significantly narrower collapse width of 5.8 cm. Despite the disparity in the failure-inducing loads between SRL-F and SRL-L, their failure modes remain fundamentally consistent. Progressive failure followed a characteristic sequence: initial rockfall from the tunnel shoulders, followed by rockfall at the tunnel crown, and subsequent rockfall from either the tunnel shoulders or hance, culminating in the ultimate collapse of the tunnel crown.

The failure progress of the AL under both full- and large-face excavations is shown in Fig. 13. At $\sigma = 60$ kPa, AL-F exhibited a localized rockfall of 0.9 c m × 0.5 cm at the tunnel crown. At load $\sigma = 80$ kPa, a more pronounced rockfall of 5.2 cm × 2.2 cm emerged at the tunnel crown of the AL-L. This trend suggests that the failure threshold for AL-F occurred at an applied load of 60 kPa, whereas AL-L withstood up to 80 kPa before failure occurred. With the progressive increase in load, the failure of the AL propagates laterally along the tunnel profile. At $\sigma = 120$ kPa, AL-F exhibited substantial deformation, with a rockfall of 14.5 cm × 4.6 cm at the left tunnel hance and a more extensive collapse of 21.2 cm × 4.9 cm spanning the right tunnel shoulder and right tunnel hance. In contrast, AL-L experienced comparatively less pronounced failure, with measured rockfalls of 8.7 cm × 1.9 cm at the left tunnel hance and 8.5 cm × 1.8 cm at the right tunnel hance. As the applied load escalated to $\sigma = 160$ kPa, the progressive failure of the AL propagated back to the tunnel crown, culminating in rockfalls of 16.7 cm × 3.2 cm for AL-F and 13.4 cm × 4.7 cm for AL-L. Ultimately, structural collapse commenced at the tunnel crown, with AL-F falling at a critical load of $\sigma = 180$ kPa, resulting in a collapse width of 18.1 cm, while AL-L withstood a higher threshold of $\sigma = 200$ kPa before failing, exhibiting a narrower collapse width of 11.2 cm. The failure mode of AL-F and AL-L followed a consistent pattern: initial crown rockfall, subsequent rockfall at the tunnel shoulder or hance, renewed crown deterioration, and final crown collapse.

The failure progress of the PAL under full- and large-face excavations is shown in Fig. 14. At an applied load of $\sigma = 100$ kPa, both PAL-F and PAL-L exhibited localized rockfall at the tunnel crown, with PAL-F sustaining a fragment of approximately 8.9 cm × 1.8 cm, while PAL-L experienced a comparatively smaller detachment of 3.8 cm × 1.7 cm. These observations suggest that the critical load threshold for the onset of failure in both PAL-F and PAL-L is $\sigma = 100$ kPa. With increasing load, the failure of PAL propagates laterally across the tunnel profile. At $\sigma = 140$ kPa, PAL-F exhibited a rockfall of approximately 6.5 cm × 2.2 cm at the left tunnel shoulder, whereas PAL-L experienced a more pronounced drop of 19.2 cm × 5.8 cm at the right tunnel shoulder. As failure progressed, the damage extended upward toward the tunnel crown. At $\sigma = 260$ kPa, PAL-F sustained a rockfall of 6.8 cm × 2.7 cm at the tunnel crown, while PAL-L exhibited a rockfall of 4.7 cm × 2.9 cm in the same region. At $\sigma = 340$ kPa, both PAL-F and PAL-L succumbed to structural failure at the tunnel crown, with collapse widths of approximately 18.9 cm and 7.7 cm, respectively. The failure mode of PAL-F and PAL-L followed a consistent pattern, characterized by initial tunnel crown rockfall, subsequent rockfall at the tunnel shoulder or hance, further deterioration at the tunnel crown, and ultimately, complete structural collapse at the tunnel crown.

The failure modes of the surrounding rock under various working conditions are shown in Fig. 15. Notably, the excavation method, whether full-face or large-face, exerted no discernible influence on the failure mode of the anchorage layer. For identical support types, the failure mode remained consistent, regardless of the excavation

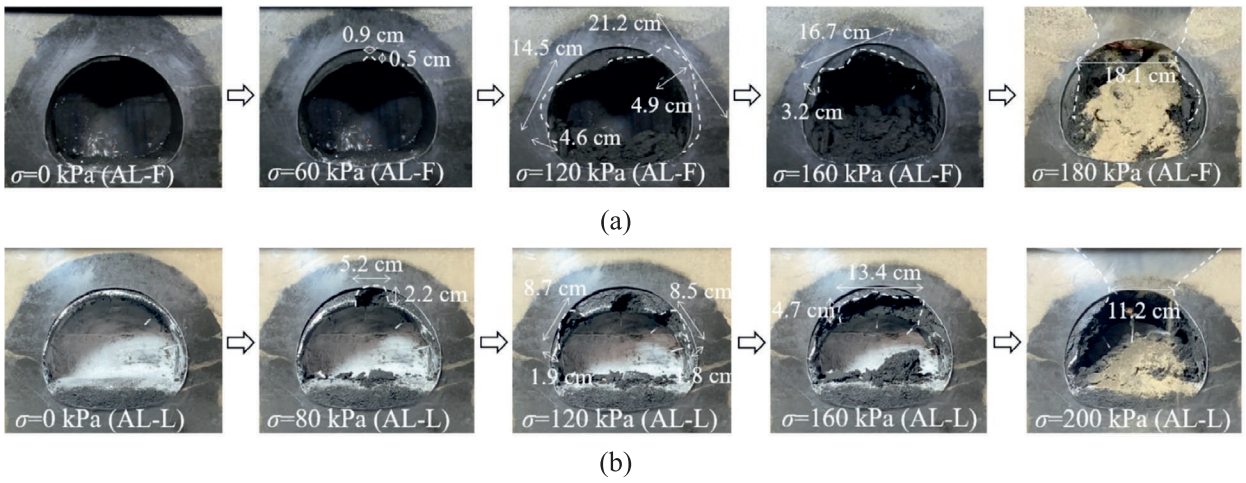

Fig. 13. Failure process of AL. (a) AL-F, and (b) AL-L.

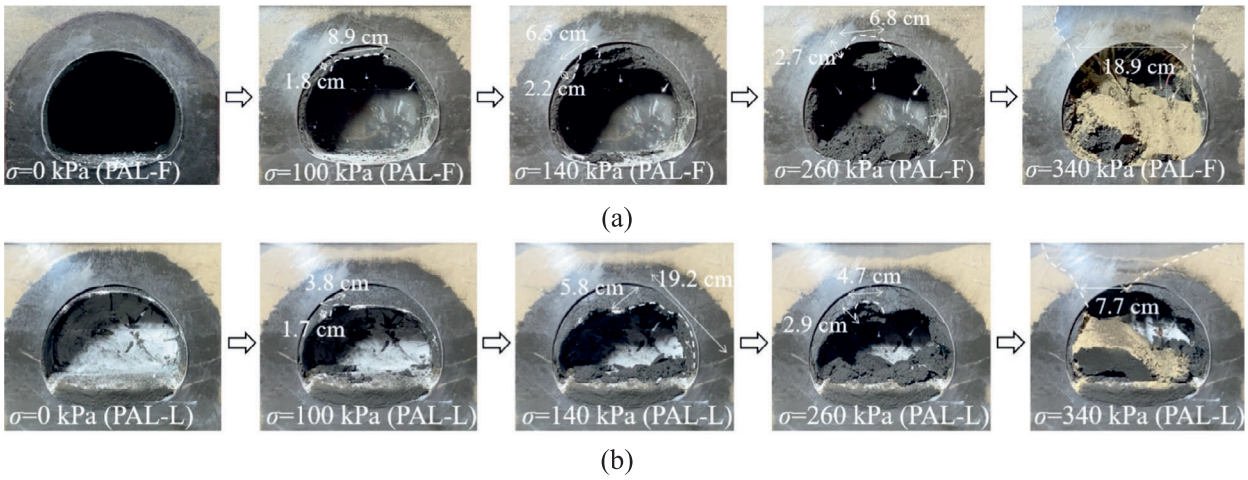

Fig. 14. Failure process of PAL. (a) PAL-F, and (b) PAL-L.

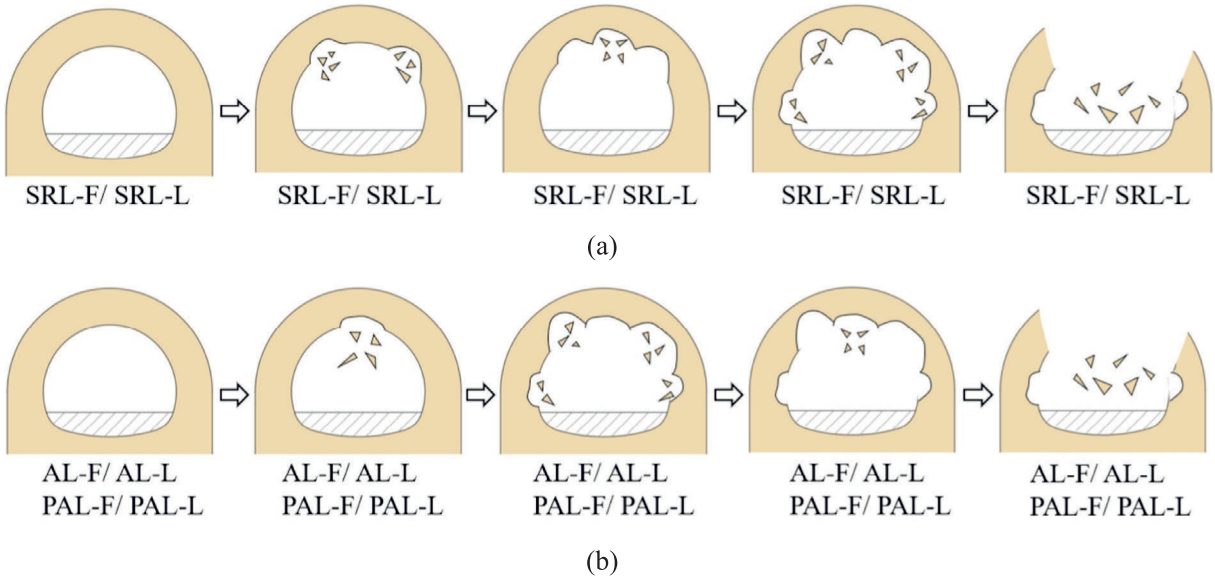

Fig. 15. Failure mode. (a) SRL-F or SRL-L, and (b) AL-F or AL-L or PAL-F or PAL-L.

approach. However, variations in the support type alter the failure modes of the anchorage layer, whereas the presence or absence of prestressing in the anchor bolts does not fundamentally alter the failure mode. The failure mode of SRL-F and SRL-L unfolded through a sequential pattern of tunnel shoulder rockfall, tunnel crown rockfall, and subsequent rockfall at the tunnel shoulder and hance, culminating in the ultimate collapse of the tunnel crown. However, the failure modes observed in AL-F, AL-L, PAL-F, and PAL-L followed a distinct trajectory characterized by initial tunnel crown rockfall, followed by rockfall at the tunnel shoulder and hance, leading to recurrent tunnel crown instability and eventual structural failure.

3.2 Displacement

As the anchorage layer undergoes failure, the particle velocity of the surrounding rock exhibits a sudden escalation, potentially introducing distortions in the PIV results. Consequently, PIV analysis of the displacement field was primarily confined to the period preceding the onset of the first rockfall. The displacement fields of SRL, AL, and PAL in the pre-failure stage are illustrated in Fig. 16. With the progressive increase in load, the displacement of the surrounding rock exhibited a gradual escalation until it reached the critical failure displacement u_f, at which point rockfall commenced. For SRL-F and SRL-L, the maximum displacement u_{max} of SRL-F at $\sigma = 20$ kPa was approximately 2.31 mm at the left and right tunnel shoulders, coinciding with the onset of rockfall. SRL-L attained a u_{max} of approximately 2.98 mm at the left tunnel shoulder at $\sigma = 40$ kPa, likewise accompanied by rockfall. Hence, the u_f values of SRL-F and SRL-L were determined to be 2.31 mm and 2.98 mm, respectively. For AL-F and AL-L, the failure displacement u_f occurred at the tunnel crown, measuring 4.33 mm at $\sigma = 60$ kPa for AL-F

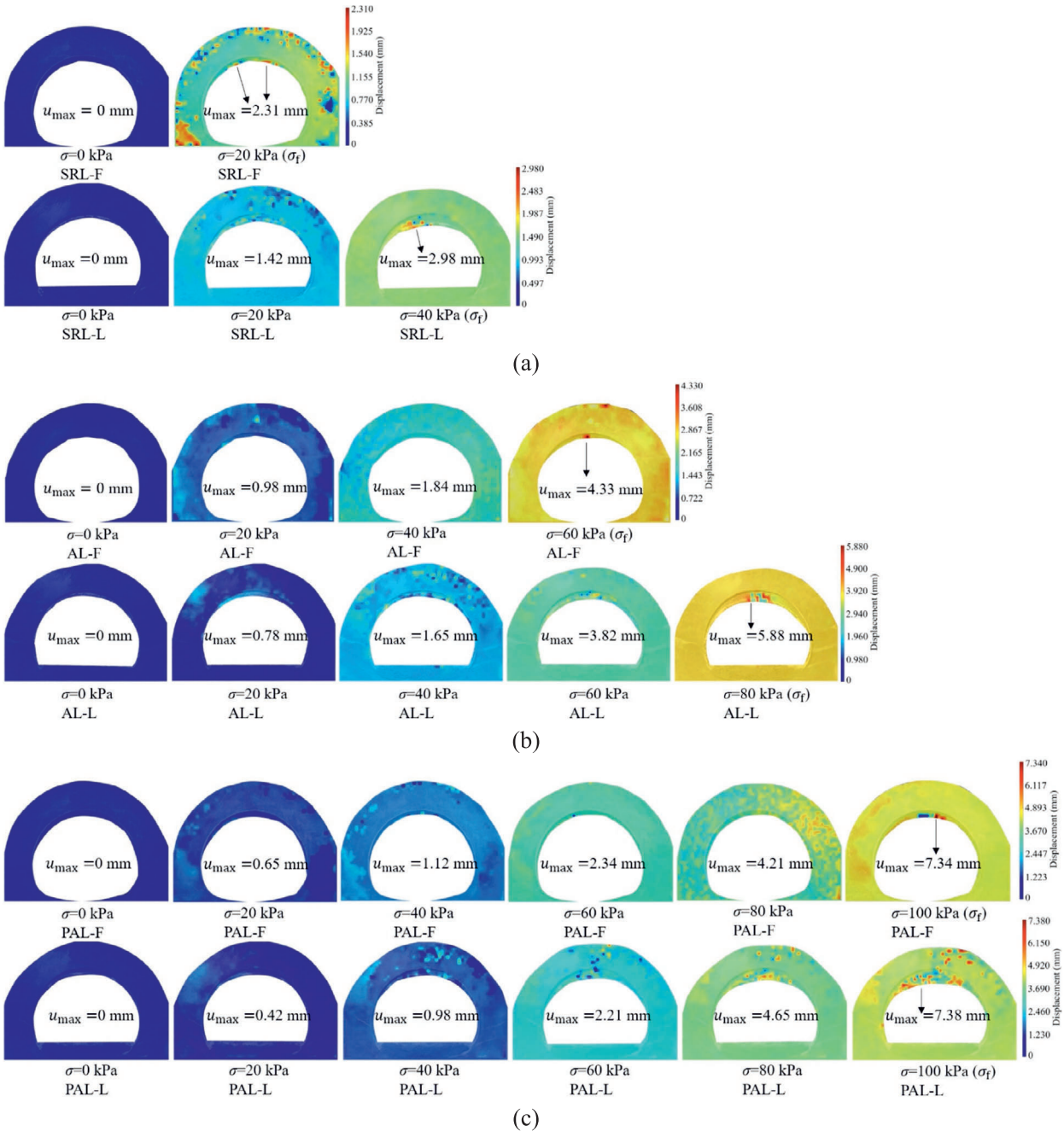

Fig. 16. Displacement field. (a) SRL, (b) AL, and (c) PAL.

and 5.88 mm at $\sigma = 80$ kPa for AL-L. In the case of PAL-F and PAL-L, the surrounding rock exhibited failure at the tunnel crown at $\sigma = 100$ kPa, with u_f values of 7.34 mm and 7.38 mm, respectively.

The variations in u_{max} and u_f under different loading and work conditions are illustrated in Fig. 17. Regarding the support types, for a given load, u_{max} within the anchorage layer decreased progressively as the support system was reinforced. At $\sigma = 40$ kPa, u_{max} for SRL-L, AL-L, and PAL-L measured 2.98 mm, 1.65 mm, and 0.98 mm, respectively, representing reductions of approximately 67.1% and 40.6% for PAL-L compared to SRL-L and AL-L. Moreover, as the support system was strengthened, the u_f of the anchorage layer exhibited a gradual increase. The values of u_f for SRL-L, AL-L, and PAL-L were 2.98 mm, 5.88 mm, and 7.38 mm, respectively, with PAL-L exhibiting an increase of approximately 147.7% and 25.5% relative to SRL-L and AL-L. This trend underscores the efficacy of anchor bolts in enhancing the ductility of the anchorage layer, thereby mitigating premature failure, whereas the application of prestress further amplifies this reinforcement effect. With regard to excavation methods, large-face excavation markedly enhanced the ductility of the surrounding rock in comparison to full-face excavation, particularly in cases where anchor support is absent or applied without prestress. The u_f values for SRL-F and SRL-L were

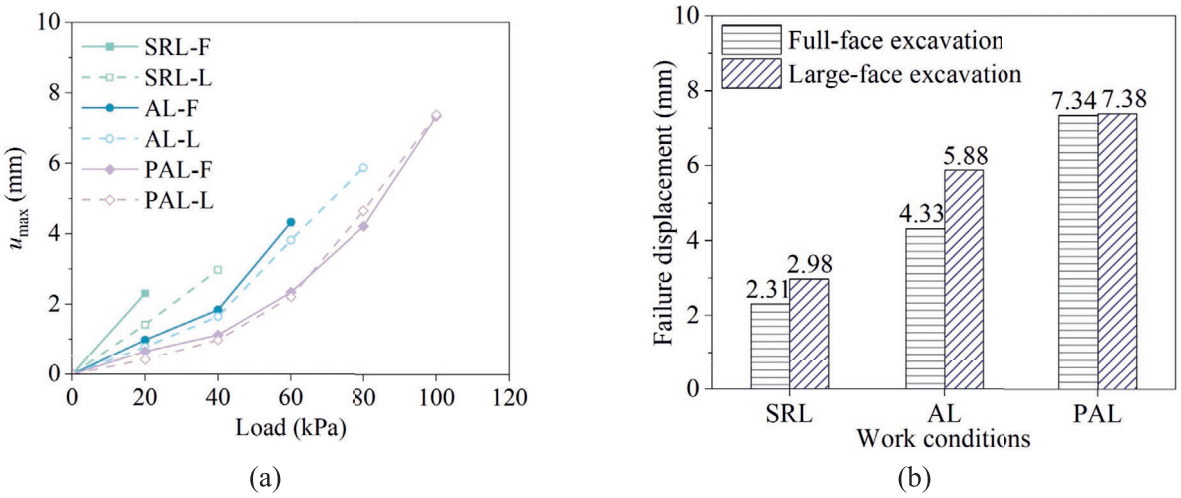

Fig. 17. Displacement under different σ. (a) u_{max}, and (b) u_f.

2.31 mm and 2.98 mm, respectively, indicating an approximate 29.1% increase in u_f for SRL-L relative to SRL-F. Similarly, for AL-F and AL-L, the corresponding values of u_f were 4.33 mm and 5.88 mm, with AL-L exhibiting a 35.8% increase over AL-F. However, when a prestressed anchor bolt support was employed, variations in the excavation method had negligible effects on the ductility of the surrounding rock. The u_f values of PAL-F and PAL-L were 7.34 mm and 7.38 mm, respectively, demonstrating an essentially identical response irrespective of the excavation approach.

3.3 Bearing capacity

To quantify the bearing capacity of the anchorage layer and assess the influence of support types and excavation methods, two critical parameters are defined: the failure load σ_f and the ultimate load σ_u. The experimental results revealed that rockfalls within the anchorage layer were typically accompanied by a pronounced concentration of displacement at the failure position, manifesting as abrupt discontinuities in the displacement field. Taking the SRL-L results as an illustrative case (see Fig. 18), when the applied load increased from 20 kPa to 40 kPa, the displacement field exhibited pronounced concentration at the left tunnel shoulder, reaching 2.98 mm and accompanied by an abrupt discontinuity. At this stage, a rockfall was similarly observed in the left tunnel shoulder. Accordingly, drawing upon existing research (Xiao et al., 2024; Yang et al., 2025) and incorporating the observed transformations in the displacement field, the σ_f of the anchorage layer is herein defined as the concurrence of the rockfall and abrupt displacement field variation. The σ_u is defined as the load that causes the anchorage layer to undergo its final collapse.

The variations in σ_f and σ_u under different work conditions are illustrated in Fig. 19. As the level of support type increased, the bearing capacity of the anchorage layer exhibited a corresponding enhancement. Specifically, the σ_f value of PAL-F peaked at 100 kPa, representing a 5 times and 1.7 times increase compared to SRL-F and AL-F, respectively, while achieving a σ_u value of 340 kPa—4.3 times and 1.9 times greater than those of SRL-F and AL-F. These findings underscore the substantial role of anchor bolts in fortifying the anchorage layer, and the application of prestress further amplified this reinforcement effect. Regarding excavation methods, the σ_f and σ_u of SRL-L were 2 times and 1.5 times those of SRL-F, respectively, whereas for AL-L, these values were 1.3 times and 1.1 times those of AL-F. Notably, the σ_f and σ_u of PAL-L remained identical to those of PAL-F. These results suggest that in the absence of an anchor bolt support, large-face excavation markedly enhanced the bearing capacity relative to full-face excavation, yielding an increase of approximately 50% to 100%. When an anchor bolt support was employed without prestressing, large-face excavation contributed to a moderate improvement in the bearing capacity, ranging from 10% to 30%. However, when a prestressed anchor bolt support was implemented, variations in the excavation methods exerted no discernible influence on the bearing capacity of the anchorage layer.

3.4 Macroscopic influence of excavation method

Drawing upon macroscopic experimental results, in the absence of an anchor bolt support or when anchor bolts were employed without prestress, large-face excavation markedly enhanced the ductility of the surrounding rock, prolonged its resistance to failure, and consequently augmented its bearing capacity. In the absence of support, large-face excavation enhanced the ductility of the surrounding rock by approximately 29.1% and increased its bearing capacity by approximately 50%–100% relative to full-face excavation. Under non-prestressed anchor bolt support, large-face excavation augmented ductility by

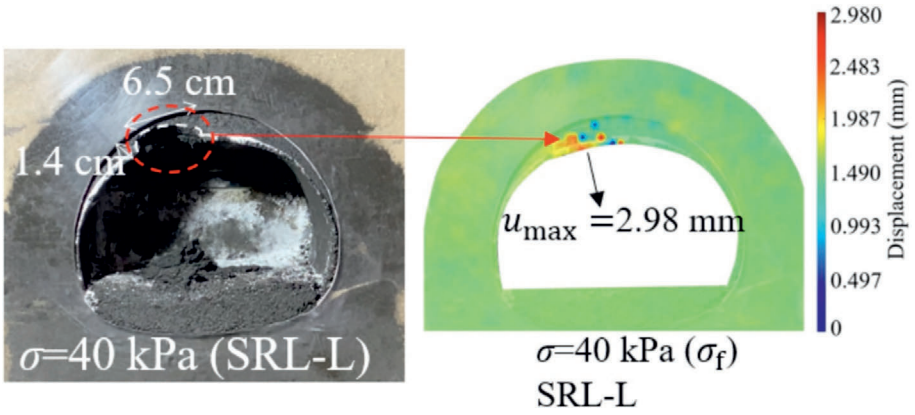

Fig. 18. Definition of the failure load.

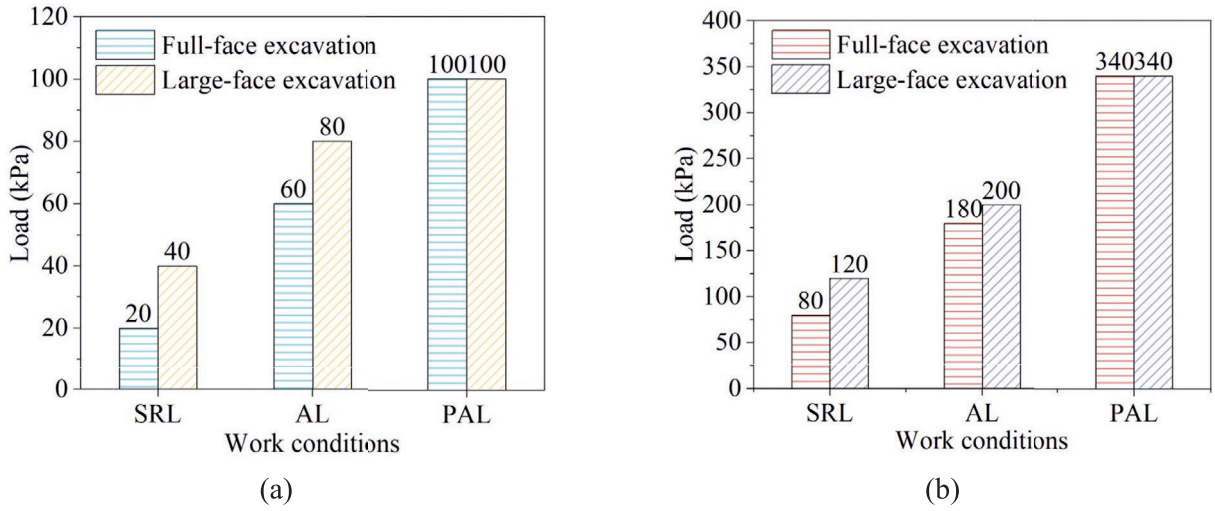

Fig. 19. (a) σ_f, and (b) σ_u.

approximately 35.8% and improved bearing capacity by approximately 10%–30% compared with the full-face method. However, when the surrounding rock was reinforced with prestressed anchor bolts, variations in the excavation method had a negligible impact on both ductility and bearing capacity.

4 Mesoscopic experimental results

4.1 Radial stress

Taking the case of $\sigma = 0$ as a representative example, the influence of support type and excavation method on the distribution of radial stress σ_r across the tunnel cross-section is elucidated in Fig. 20. With respect to support type, a progressive enhancement in σ_r is observed at identical measurement locations as the support system is fortified. At the TC-2 monitoring point, the σ_r for SRL-F, AL-F, and PAL-F were recorded as 1.10, 1.89, and 3.80 kPa, respectively—representing increases of approximately 71.8% and 245.5% for AL-F and PAL-F relative to SRL-F. These findings indicate that the installation of anchor-bolt reinforcement substantially augments the stress distribution within the surrounding rock, with prestressed anchor bolts delivering a notably superior enhancement effect. With regard to excavation methods, the adoption of large-face excavation in both SRL and AL schemes yielded elevated σ_r levels in the surrounding rock compared to full-face excavation. At the TC-2 measurement point, the σ_r for SRL-L reached 1.51 kPa, approximately 37.3% higher than the 1.10 kPa recorded for SRL-F. Similarly, AL-L exhibited a σ_r of 2.12 kPa, surpassing that of AL-F by approximately 12.2%. In contrast, for the PAL configuration, the σ_r value remained effectively unchanged between the two excavation methods, with PAL-F and PAL-L recording values of 3.80 and 3.99 kPa, respectively—a marginal difference of 5%. This observation suggests that in the absence of support or when employing non-prestressed anchor-bolt reinforcement, large-face excavation enhances the stress distribution within the surrounding rock relative to full-face excavation. However, when prestressed anchor bolts are used, the influence of the excavation method on the stress distribution becomes negligible.

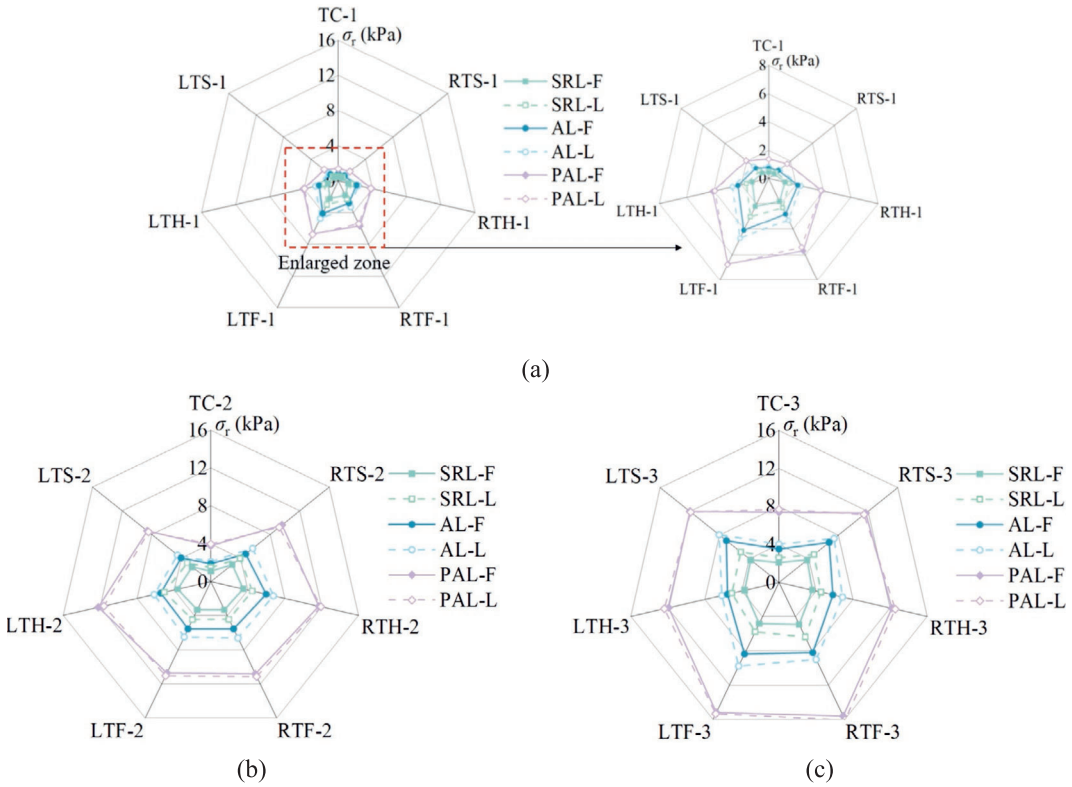

Fig. 20. σ_r at $\sigma = 0$ kPa. (a) TC-1, (b) TC-2, and (c) TC-3.

Taking measuring point TC-2 as a representative example, the time-history curves of σ_r under varying loading conditions across different work conditions are depicted in Fig. 21. Across varying load conditions, the σ_r values of SRL-L and AL-L consistently exceed those observed in SRL-F and AL-F, respectively. In contrast, the time-history curves of σ_r for PAL-F and PAL-L exhibit near-identical trends, indicating minimal sensitivity to the excavation method under prestressed anchorage. Moreover, the evolution of σ_r reveals distinct patterns among the support types. For both SRL and AL, σ_r exhibits an initial increase followed by a subsequent decline, whereas in the case of PAL, the stress rises, plateaus, and then diminishes. Specifically, for AL-F, σ_r progressively ascends from $\sigma = 0$ kPa to $\sigma = 80$ kPa, reaching a peak of 13.70 kPa, before declining to 5.10 kPa as localized rockfall ensues between 80 and 160 kPa. In contrast, PAL-F displays a more resilient response: σ_r climbs steadily to 52.80 kPa over the 0–140 kPa range, remains relatively stable from 140 to 200 kPa, and only begins to recede—eventually falling to 24.7 kPa—once failure initiates between 200 and 260 kPa. The presence of a stable stress phase in the PAL further attests to the enhanced ductility of the surrounding rock conferred by the application of prestressed anchor bolts.

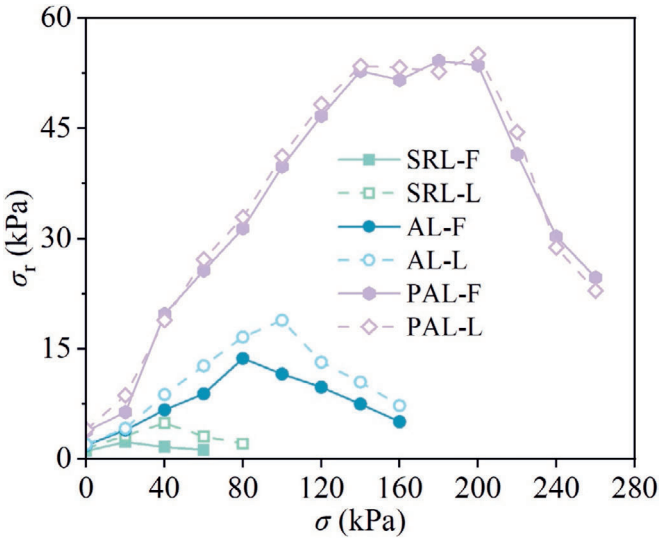

Fig. 21. σ_r at TC-2 under different σ.

4.2 Integrity

To elucidate the evolution of P-wave velocity V_p and the integrity K_v of the surrounding rock, and to identify the critical thresholds marking rock failure, the variations of V_p and K_v under differing σ are depicted in Fig. 22 and Fig. 23. The K_v value was derived from Eq. (1). Both V_p and K_v exhibit a declining trend at the tunnel crown and shoulders, accompanied by a gradual increase at the tunnel hance, as the external load σ intensifies along the tunnel

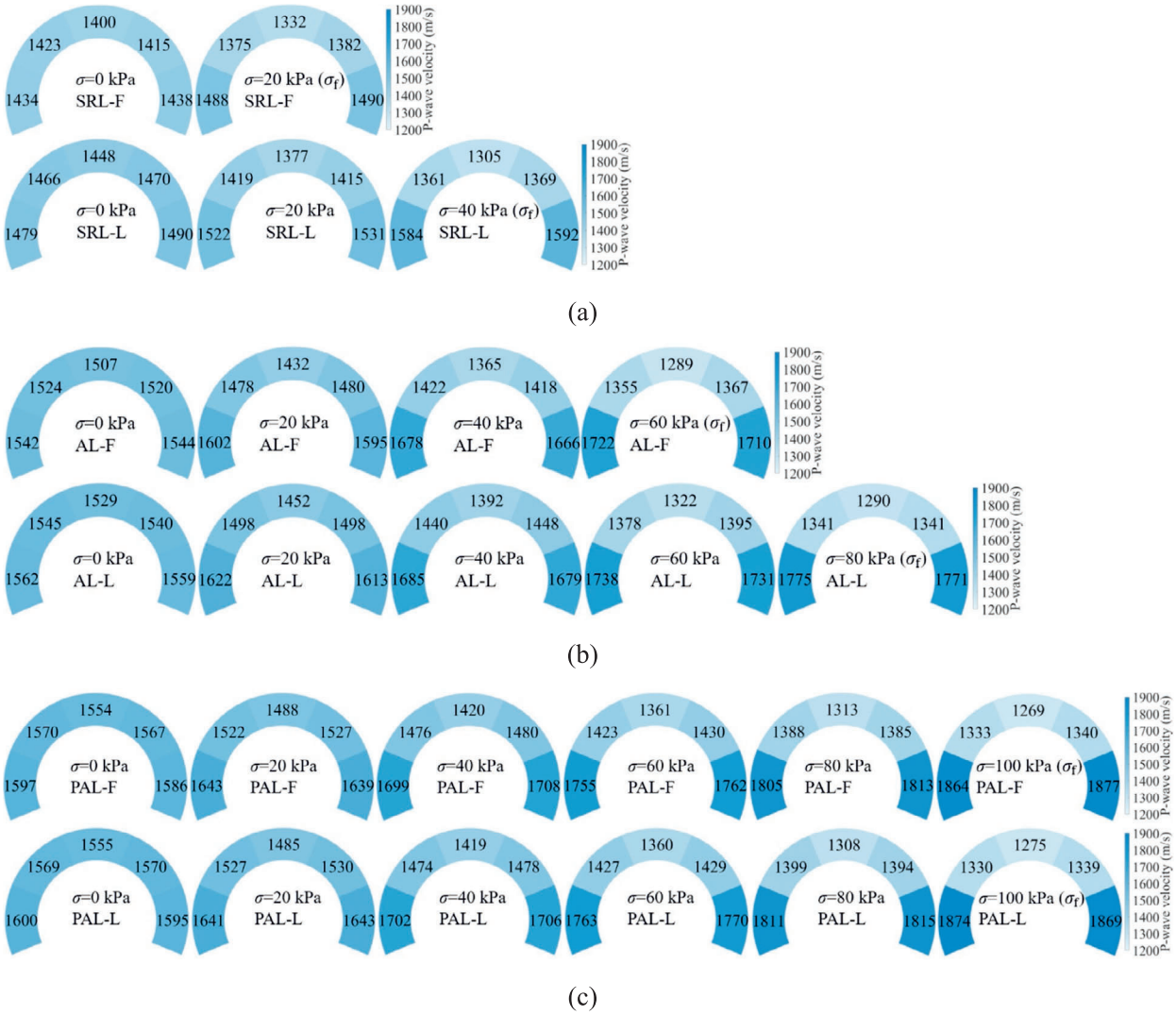

Fig. 22. P-wave velocity field. (a) SRL, (b) AL, and (c) PAL.

cross-section. Taking SRL-L as a representative case, at $\sigma = 0$, the V_p and K_v values at the tunnel crown were 1448 m/s and 0.46, respectively. Upon increasing the load to $\sigma = 40$ kPa, these values diminish to 1305 m/s and 0.37, reflecting reductions of approximately 9.9% and 19.6%, respectively. Conversely, the tunnel height increased by approximately 7.1% in V_p and 14.6% in K_v. This spatial redistribution suggests progressive loosening of the rock mass at the tunnel crown and shoulders under loading, thereby rendering these regions increasingly susceptible to rockfalls and failures. At the critical load of $\sigma = 40$ kPa in the SRL-L configuration, rockfall was observed at the left tunnel shoulder. At this point, the corresponding V_p and K_v values were 1361 m/s and 0.41, respectively. These values were identified as the failure threshold parameters, denoted as the failure P-wave velocity $V_{pf} = 1361$ m/s and failure integrity $K_{vf} = 0.41$. Similarly, the V_{pf} and K_{vf} values for SRL-F were determined to be 1375 m/s and 0.41, respectively. For AL-F and AL-L, the corresponding V_{pf} values were 1289 and 1290 m/s, respectively, with both exhibiting a K_{vf} of 0.36. In the case of PAL-F and PAL-L, the V_{pf} value was measured at 1269 and 1275 m/s, with corresponding K_{vf} values of 0.35 and 0.36, respectively.

Taking the tunnel crown as a representative location, the variations in V_p and K_v under different loading conditions are depicted in Fig. 24, elucidating the influence of the excavation methods and support types on the V_p and K_v of the surrounding rock. In terms of the excavation method, both the V_p and K_v of SRL-L and AL-L consistently exceeded those of their full-face excavations, SRL-F and AL-F, across varying load levels. In contrast, PAL-F and PAL-L exhibited nearly identical V_p and K_v. For instance, at $\sigma = 20$ kPa, the V_p and K_v of SRL-L surpass those of SRL-F by approximately 3.4% and 7.7%, respectively, while AL-L shows respective increases of 1.4% and 2.2% over AL-F. Conversely, the discrepancy between PAL-F and PAL-L is negligible, with a mere 0.2% variation in V_p and identical K_v. These observations underscore that in the absence of prestressed anchor bolts,

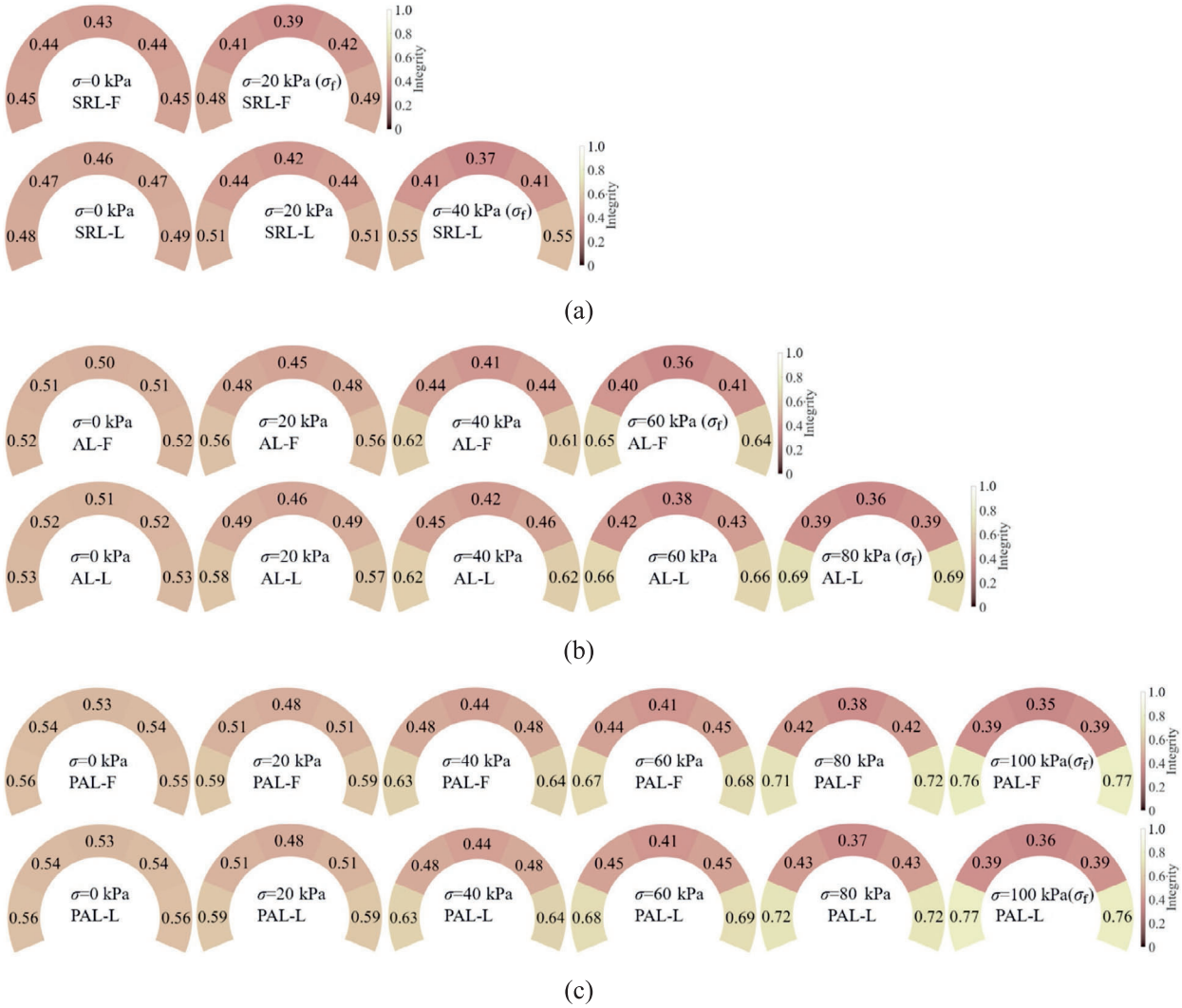

Fig. 23. Integrity field. (a) SRL, (b) AL, and (c) PAL.

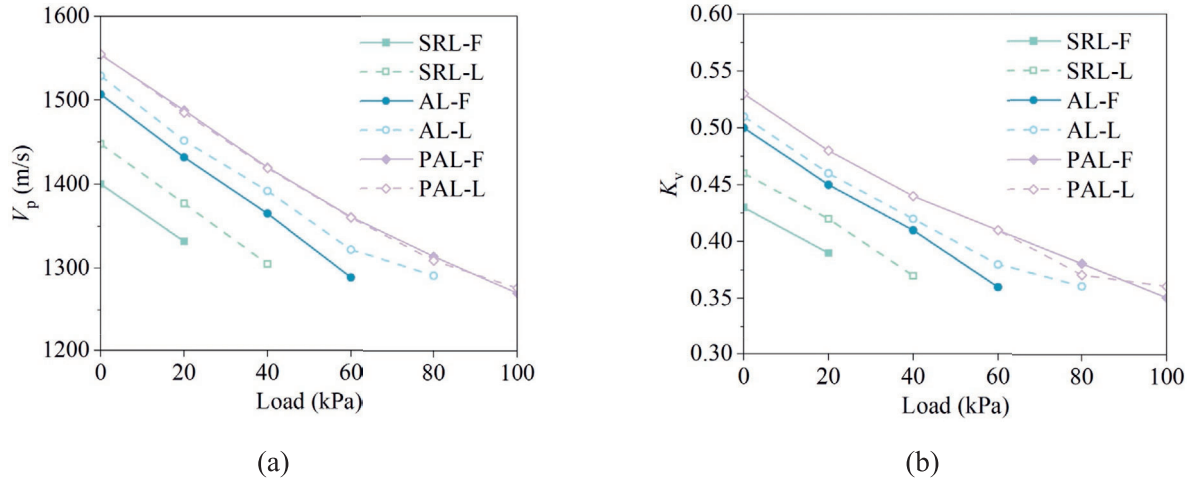

Fig. 24. (a) V_p, and (b) K_v at tunnel crown under different σ.

large-face excavation can enhance the V_p and K_v of the surrounding rock relative to full-face excavation. However, this advantage diminishes when prestressed anchor bolts are employed, making the influence of the excavation method marginal. With respect to the support types, the incorporation of prestressed anchor bolts markedly

enhanced both V_p and K_v of the surrounding rock. At a confining pressure of $\sigma = 20$ kPa, the V_p of PAL-L exceeded that of AL-L and SRL-L by 2.3% and 7.8%, respectively, while its K_v was elevated by 4.3% and 14.3%.

4.3 Mechanical properties

To further elucidate the influence of the excavation method on the mechanical properties of the surrounding rock from a mesoscopic perspective, the elastic modulus E and cohesion c were derived from the P-wave velocity through the established conversion relationships. These derivations, grounded in the elastic wave equation and informed by Zhang et al. (2024), are presented in Eqs. (2) and (3). Figure 25 illustrates the spatial distribution and evolutionary trend of E within the surrounding rock under various load conditions. With an increasing load, E at the tunnel crown and shoulder exhibited a progressive decline, whereas E at the tunnel height showed a gradual enhancement. For instance, under the SRL-L condition, as the load increased from 0 to 40 kPa, the E at the tunnel crown declined from 60.85 MPa to 49.42 MPa, representing a reduction of approximately 18.8%. In contrast, E at the tunnel hance rose from 63.48 MPa to 72.81 MPa, corresponding to an increase of about 14.7%. Likewise, c of the surrounding rock exhibits the following trend: it increases progressively with increasing load at the tunnel crown and shoulder, whereas at the tunnel height, c diminishes as the load intensifies, as shown in Fig. 26. In the case of SRL-L, as the load rises from 0 to 40 kPa, the c at the tunnel crown declines from 11.52 kPa to 10.31 kPa, representing a reduction of approximately 10.5%. By contrast, at the tunnel hance, c increases from 11.85 kPa to about 13.19 kPa, corresponding to an enhancement of roughly 11.3%.

$$E = \frac{\rho(1+v)(1-2v)}{1-v} V_p^2 \frac{C_{V_p}}{C_E}, \tag{2}$$

$$c = -2.93V_p^{4.12} + 3.37V_p^{4.28} + 8.55, \tag{3}$$

where v and ρ are the Poisson's ratio and density of the surrounding rock, respectively.

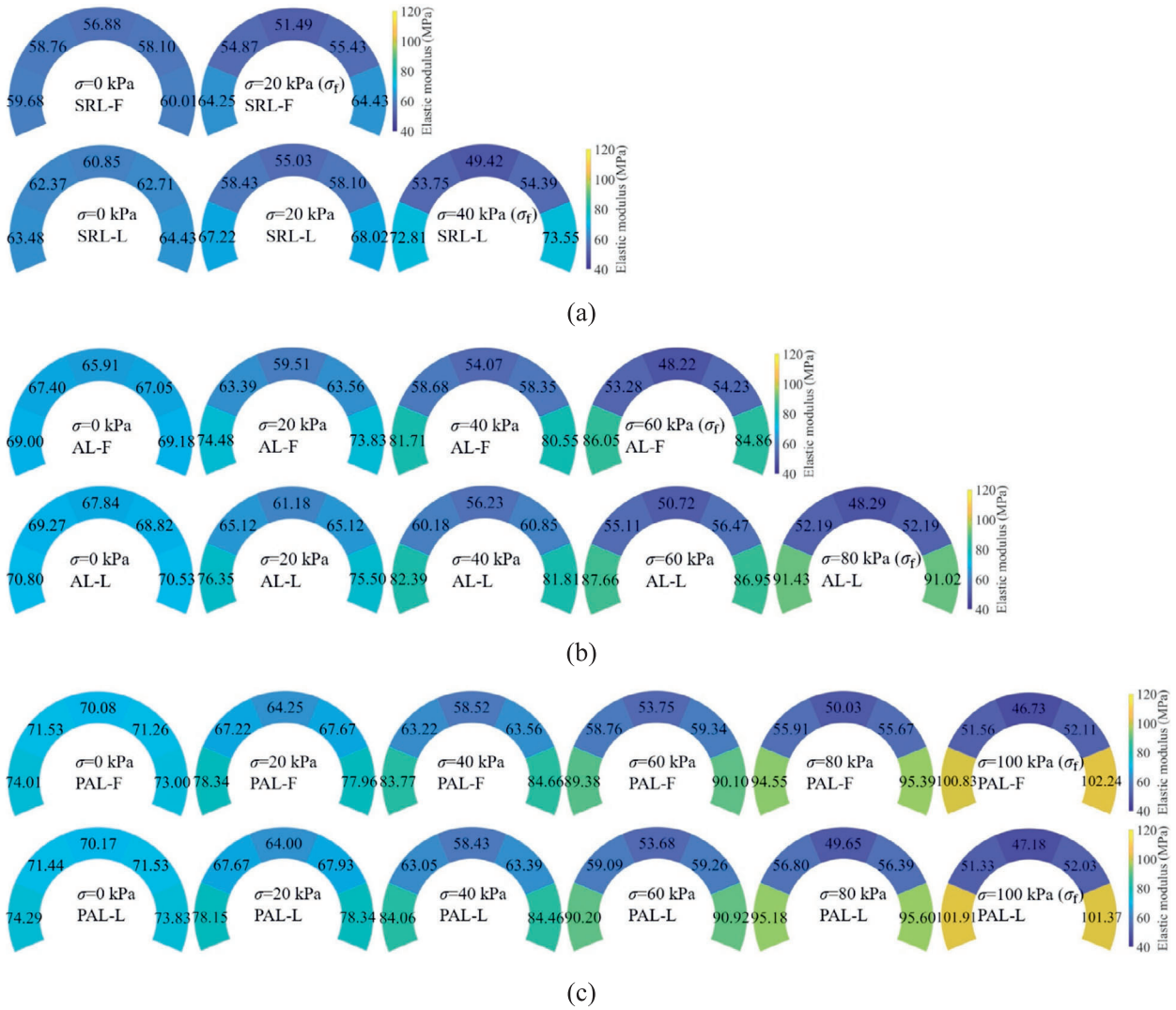

Fig. 25. Elastic modulus field. (a) SRL, (b) AL, and (c) PAL.

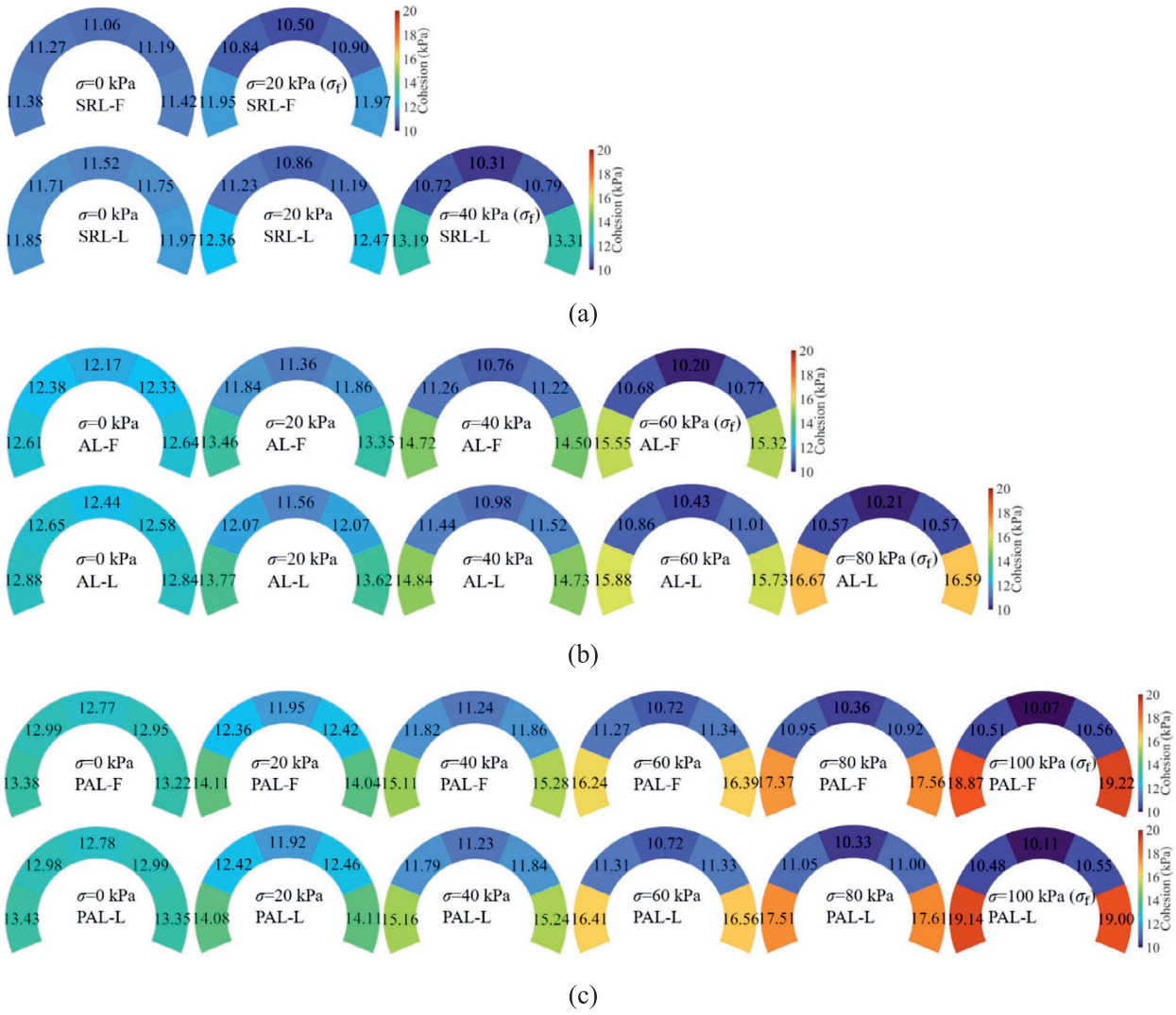

Fig. 26. Cohesion modulus field. (a) SRL, (b) AL, and (c) PAL.

Using the tunnel crown as a representative case, we examined the impact of the excavation methods and support types on E and c of the surrounding rock, as depicted in Fig. 27. Regarding the excavation methods, the E and c values of SRL-L and AL-L exceeded those of SRL-F and AL-F, respectively, whereas PAL-F and PAL-L exhibited negligible differences. This suggests that large-face excavation without prestressed anchor bolts enhances the mechanical properties of the surrounding rock compared with full-face excavation, whereas the distinction between the two methods diminishes when prestressed anchor bolts are employed. At 20 kPa, the ratios of E and c for SRL-L relative to SRL-F were approximately 6.9% and 3.4%, respectively, whereas the corresponding ratios for AL-L compared with AL-F were 2.8% and 1.8%, respectively. In contrast, PAL-F and PAL-L demonstrated virtually identical performance. Regarding the support types, the installation of anchor bolts enhanced the mechanical properties of the surrounding rock, with prestressed anchor bolts exhibiting a more pronounced reinforcing effect. At a pressure of 20 kPa, E for PAL-L demonstrated increases of 4.6% and 16.3% relative to AL-L and SRL-L, respectively, while the corresponding improvements in c were approximately 3.1% and 9.8%, respectively.

4.4 Mesoscopic influence of excavation method

Drawing on mesoscopic experimental analyses, in the absence of prestressed anchor bolts, large-face excavation optimizes the stress distribution and improves the integrity relative to full-face excavation, thereby enhancing the mechanical properties of the surrounding rock. In the absence of support, the large-face excavation enhanced the surrounding rock stress by approximately 37.3%, elevated the integrity by approximately 7.7%, and improved the mechanical properties by approximately 6.9% relative to the full-face excavation. Under a non-prestressed anchor bolt support, large-face excavation further increases rock stress by approximately 12.2% while enhancing integrity by approximately 2.2% and mechanical properties by

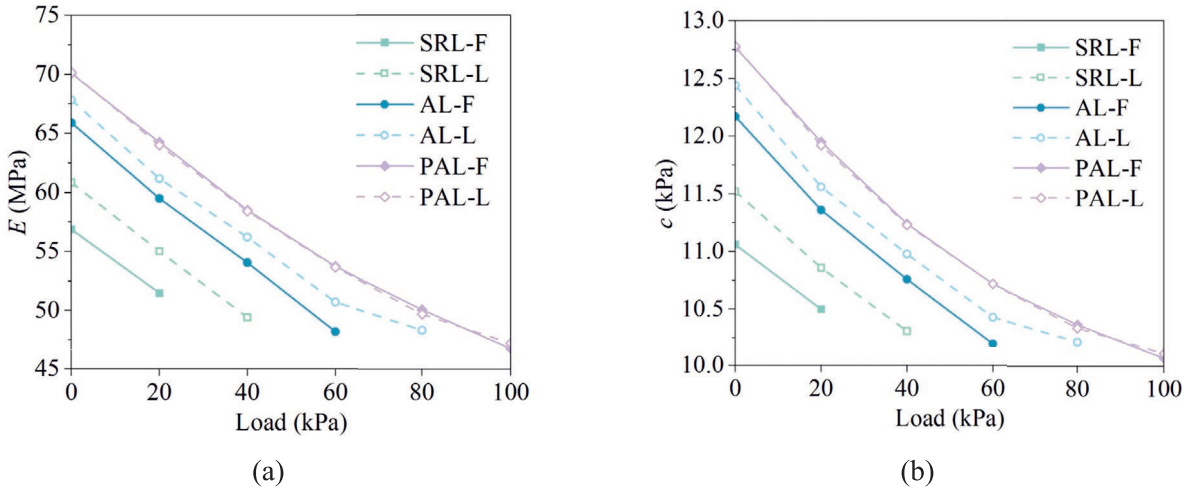

Fig. 27. E and c at the tunnel crown under different σ. (a) E, and (b) c.

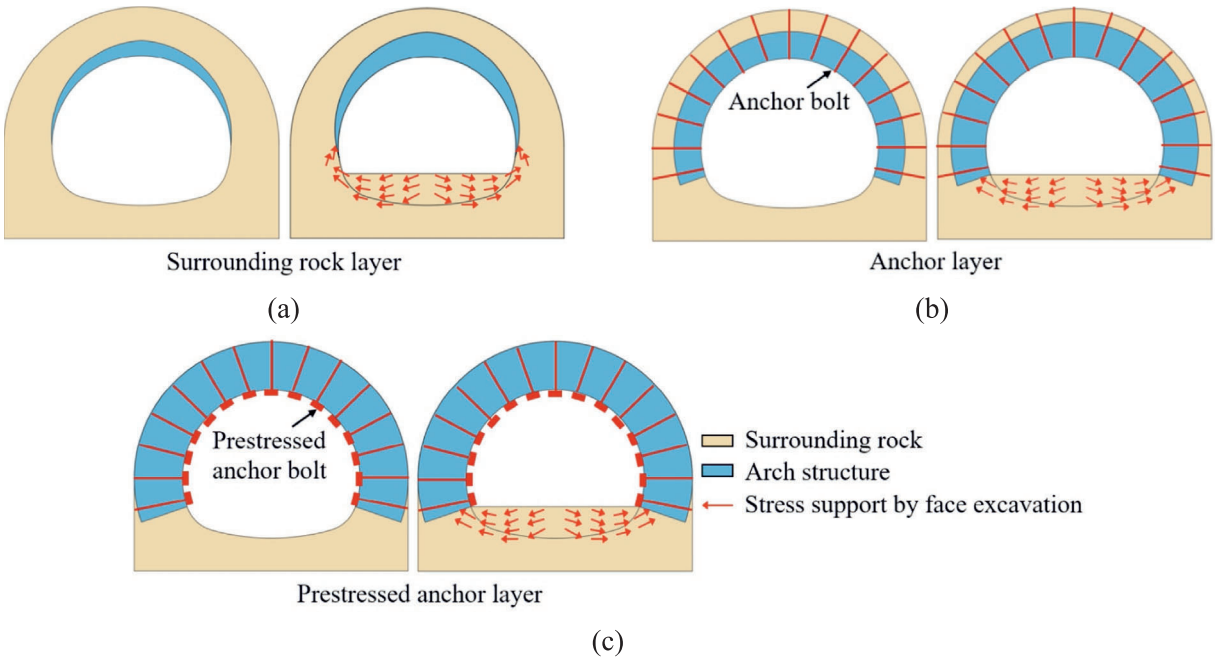

Fig. 28. Mechanism differences between large-face and full-face excavation. (a) SRL, (b) AL, and (c) PAL.

approximately 2.8% when compared to the full-face method. Conversely, when prestressed anchor bolts are employed, the disparities in stress distribution, integrity, and mechanical properties between the large-face and full-face excavation methods become statistically negligible.

5 Discussion

The experimental findings underscore the pronounced efficacy of prestressed anchor bolts in enhancing the behavior of the surrounding rock from both mesoscopic and macroscopic perspectives. From a mesoscopic perspective, the application of a prestressed anchor bolt markedly elevated the radial stress, integrity, and mechanical properties, registering improvements of approximately 245.5%, 14.3%, and 9.8%, respectively, compared with the unsupported condition. Macroscopically, the use of the prestressed anchor bolt yielded substantial gains in both ductility and bearing capacity, with increases of approximately 147.7% and 500%, respectively, compared with scenarios lacking support. The reinforcement mechanism of prestressed anchor bolts may be delineated as a progressive multiscale enhancement process. Initially, they elevate the stress state of the surrounding rock; subsequently, they promote integrity and augment mechanical properties, such as elastic

modulus and cohesion, which ultimately coalesce to substantially enhance the ductility and bearing capacity of the rock mass at the macroscopic scale.

With respect to the excavation methods, in the absence of prestressed anchor-bolt reinforcement, large-face excavation enhanced the stress distribution, integrity, mechanical properties, ductility, and bearing capacity of the surrounding rock relative to full-face excavation by approximately 12.2%, 37.3%, 2.2% to 7.7%, 2.8%, 6.9%, 29.1%, 35.8%, and 50% to 100%, respectively. However, when prestressed anchor bolts were employed, the influence of the excavation method on these parameters became negligible. This phenomenon can be attributed to the internal redistribution of stress within the surrounding rock following tunnel excavation, which naturally gives rise to an arch structure that contributes to overall stability. In cases lacking support or employing anchor bolts, large-face excavation preserves the tunnel invert and effectively extends the range of the arch structure. This configuration offered enhanced stress support to the overlying rock mass, thereby improving the stress, integrity, mechanical properties, ductility, and bearing capacity, as illustrated in Fig. 28 (a) and (b). However, when prestressed anchor bolts were employed, the additional stress support of the tunnel invert became negligible. Consequently, the mesoscopic and macroscopic characteristics of the surrounding rock remained largely unchanged, as shown in Fig. 28(c).

Based on the experimental findings, we recommend that tunnel construction adopt anchor bolts, preferably in their prestressed form, for the reinforcement of the surrounding rock. Such measures markedly enhance the bearing capacity while ensuring stability. Under unsupported conditions, or when employing conventional anchor bolt supports, a large-face excavation method is recommended for tunnel construction. However, when prestressed anchor bolt support systems are utilized, a full-face excavation approach is preferred.

6 Conclusions

This study investigated the influence of two excavation methods—full-face and large-face—through a series of loading and failure experiments aimed at elucidating both the macroscopic bearing capacity and microscopic mechanical properties of the anchorage layer. The principal findings are summarized as follows.

(1) The excavation method did not alter the failure mode of the anchorage layer. Both full- and large-face excavations exhibited consistent failure modes under identical support conditions. In contrast, the support type significantly affected the failure mode. In the absence of supports, failure typically initiates at the tunnel shoulder, whereas the presence of conventional or prestressed anchor bolts shifts the initial failure locus to the tunnel crown.

(2) The reinforcement of the surrounding rock using prestressed anchor bolts unfolds as a progressive enhancement process, beginning with the improvement in stress, followed by an increase in integrity and mechanical properties, culminating in a pronounced enhancement of ductility and bearing capacity from a macroscopic perspective. Compared to the unsupported conditions, the application of prestressed anchor bolts yielded substantial gains: approximately 245.5% in stress, 14.3% in integrity, 9.8% in mechanical properties, 147.7% in ductility, and a remarkable overall bearing capacity.

(3) In the absence of prestressed anchor bolts, large-face excavation significantly enhanced the performance of the anchorage layer relative to full-face excavation by 12.2%–37.3%, integrity by 2.2%–7.7%, mechanical properties by 2.8%–6.9%, ductility by 29.1%–35.8%, and bearing capacity by 50%–100%. However, when the prestressed anchor bolts were employed, the differences between the two excavation methods became negligible.

(4) For tunnels lacking support or employing anchor bolts, a large-face excavation is preferable. Conversely, a full-face excavation is advised under the reinforcement of prestressed anchor bolts.

Data availability

The data that support the findings of this study are available from the corresponding author upon reasonable request.

CRediT authorship contribution statement

Henghong Yang: Writing – original draft, Methodology, Formal analysis, Data curation, Conceptualization. **Mingnian Wang:** Writing – review & editing, Supervision, Project administration, Funding acquisition, Conceptualization. **Li Yu:** Project administration, Funding acquisition, Conceptualization. **Jie Liu:** Visualization, Formal analysis, Data curation. **Xiao Zhang:** Visualization, Formal analysis, Data curation. **Zhihui Xu:** Visualization, Data curation. **Jun Liu:** Visualization, Data curation.

Declaration of competing interest

The authors declare that they have no known competing financial interests or personal relationships that could have appeared to influence the work reported in this paper.

Acknowledgement

The authors are grateful for the supports from the National Natural Science Foundation of China (Grant Nos. 52208404 and 52378411), Doctoral Innovation Fund Program of Southwest Jiaotong University (Grant No.

CX2025YB01), Fundamental Research Funds for the Central Universities (Grant No. 2682024CX020), China National Railway Group Limited Science and Technology Research and Development Program (Grant No. K2023G041), Technology Program of Chengdu (Grant No. 2022-XT00-00002-GX), China Postdoctoral Science Foundation (Grant No. 2023M742898), the Postdoctoral Fellowship Program of China Postdoctoral Science Foundation (Grant No. GZC20232193), and the Natural Science Foundation of Sichuan (Grant No. 24NSFSC7133), China.

References

Carranza-Torres, C. (2009). Analytical and numerical study of the mechanics of rockbolt reinforcement around tunnels in rock masses. *Rock Mechanics and Rock Engineering, 42*(2), 175–228.

Chen, J., Hagan, P. C., & Saydam, S. (2016). Load transfer behavior of fully grouted cable bolts reinforced in weak rocks under tensile loading conditions. *Geotechnical Testing Journal, 39*(2), 252–263.

Chen, J., Saydam, S., & Hagan, P. C. (2018). Numerical simulation of the pull-out behaviour of fully grouted cable bolts. *Construction and Building Materials, 191*, 1148–1158.

Chen, Y., Teng, J., Sadiq, R. A. B., & Zhang, K. (2020). Experimental study of bolt-anchoring mechanism for bedded rock mass. *International Journal of Geomechanics, 20*(4), 0001561.

Deb, D., & Das, K. C. (2011). Modelling of fully grouted rock bolt based on enriched finite element method. *International Journal of Rock Mechanics and Mining Sciences, 48*(2), 283–293.

Dong, E., & Wang, W. (2020). Study on anchorage failure and bolting measures of roadway in weak rock. *Geotechnical and Geological Engineering, 38*(1), 997–1012.

Elrawy, W. R., Abdelhaffez, G. S., & Saleem, H. A. (2020). Stability assessment of underground openings using different rock support systems. *The Mining-Geology-Petroleum Engineering Bulletin, 35*(1), 49–63.

He, L., An, X., & Zhao, Z. (2015). Fully grouted rock bolts: An analytical investigation. *Rock Mechanics and Rock Engineering, 48*(3), 1181–1196.

Ho, D. A., Bost, M., & Rajot, J. P. (2019). Numerical study of the bolt-grout interface for fully grouted rockbolt under different confining conditions. *International Journal of Rock Mechanics and Mining Sciences, 119*, 168–179.

Hoek, E., & Brown, E. (1980). Underground excavations in rock. *CRC Press*. https://doi.org/10.1201/9781482288926.

Høien, A. H., Li, C. C., & Zhang, N. (2021). Pull-out and critical embedment length of grouted rebar rock bolts-mechanisms when approaching and reaching the ultimate load. *Rock Mechanics and Rock Engineering, 54*(3), 1431–1447.

Hu, Y., Zheng, M., Feng, W., Tong, J., Wang, Y., Wang, Q., Liu, K., & Ye, L. (2023). Interface bond degradation and damage characteristics of full-length grouted rock bolt in tunnels with high temperature. *Journal of Rock Mechanics and Geotechnical Engineering, 15*(10), 2639–2657.

Hyett, A., Bawden, W., & Reichert, R. (1992). The effect of rock mass confinement on the bond strength of fully grouted cable bolts. *International Journal of Rock Mechanics and Mining Sciences & Geomechanics Abstracts, 29*(5), 503–524.

Jing, H., Yang, S., Zhang, M., Xu, G., & Chen, K. (2014). An experimental study on anchorage strength and deformation behavior of large-scale jointed rock mass. *Tunnelling and Underground Space Technology, 43*, 184–197.

Lang, T. (1961). Theory and practice of rock bolting. *Transactions of the American Institute of Mining, Metallurgical Petroleum Engineers, 220*, 333–348.

Li, Y., Li, C., Zhang, L., Zhu, W., Li, S., & Liu, J. (2017). An experimental investigation on mechanical property and anchorage effect of bolted jointed rock mass. *Geosciences Journal, 21*(2), 253–265.

Liu, X., Yao, Z., Cheng, H., & Zha, W. (2023). Experimental study and mechanism analysis of bolt anchorage interface failure under temperature and pressure coupling. *International Journal of Adhesion and Adhesives, 126*, 103488.

Ma, H., Tan, X., Qian, J., & Hou, X. (2019). Theoretical analysis of anchorage mechanism for rock bolt including local stripping bolt. *International Journal of Rock Mechanics and Mining Sciences, 122*, 104080.

Martin, L. (2012). *Theoretical and experimental study of fully grouted rockbolts and cablebolts under axial loads*. Paris, France: Paris Institute of Technology (PhD Thesis).

National Railway Administration of the People's Republic of China (2014). *Code for design of High speed railway (TB 10621—2014)*. Beijing: China Railway Publishing House (in Chinese).

Singh, P., Spearing, A. S., Jessu, K., & Da Silva Ribeiro, P. C. P. (2020). Establishing the need to model the actual state of stress along rock bolts. *International Journal of Mining Science and Technology, 30*(3), 279–286.

Skrzypkowski, K., Korzeniowski, W., Zagórski, K., & Zagórska, A. (2020). Modified rock bolt support for mining method with controlled roof bending. *Energies, 13*(8), 1868.

Srivastava, L. P., & Singh, M. (2015). Effect of fully grouted passive bolts on joint shear strength parameters in a blocky mass. *Rock Mechanics and Rock Engineering, 48*(3), 1197–1206.

Sun, B., Liu, Q., Li, W., Yang, X., Yang, B., & Li, T. (2022). Numerical implementation of rock bolts with yield and fracture behaviour under tensile-shear load. *Engineering Failure Analysis, 139*, 106462.

Tang, L., Yu, L., Luo, X., Zhou, J., Li, Z., Yang, H., & Xiao, Y. (2023). Shaking table test on the seismic response and reinforcement measures of double-arch tunnels in mountainous areas. *Tunnelling and Underground Space Technology, 139*, 105232.

Thielicke, W., & Stamhuis, E. (2014). PIVlab–towards user-friendly, affordable and accurate digital particle image velocimetry in MATLAB. *Journal of Open Research Software, 2*.

Wang, Q., Pan, R., Li, S., Wang, H., & Jiang, B. (2018). The control effect of surrounding rock with different combinations of the bolt anchoring lengths and pre-tightening forces in underground engineering. *Environmental earth sciences, 77*(13), 501.

Wei, Z., & Zhu, Y. (2021). Seepage in water-rich loess tunnel excavating process and grouting control effect. *Geofluids, 2021*, 5597845.

Xiao, M., Xu, C., Cui, L., Sheng, Q., Chen, J., Xie, B., & Yan, Q. (2024). Experimental study on bearing capacity of systematic bolt support based on total safety factor method. *Rock and Soil Mechanics, 45*(6), 1743–1754 (in Chinese).

Yang, H., Wang, M., Yu, L., Zhang, X., Wang, Z., & Liu, D. (2025). Failure response and beam effect of bolt reinforced layer: Numerical modelling using FDM-DEM coupling method. *Engineering Failure Analysis, 175*, 109562.

Yu, W., Wang, B., Zi, X., Guo, X., & Wang, Z. (2023). Effect of prestressed anchorage system on mechanical behavior of squeezed soft rock in large-deformation tunnel. *Tunnelling and Underground Space Technology, 131*, 104782.

Zhang, D., Yang, J., & Wang, H. (2024). A novel method for predicting geomechanical parameters of gassy sediments: Insights from theoretical models and laboratory testing. *Geoenergy Science and Engineering, 243*, 213336.

Zuo, J., Wen, J., Li, Y., Sun, Y., Wang, J., Jiang, Y., & Liu, L. (2019). Investigation on the interaction mechanism and failure behavior between bolt and rock-like mass. *Tunnelling and Underground Space Technology, 93*, 103070.